DISCLAIMER

INL/RPT-25-88176
Revision 1

Nuclear Energy Advanced Modeling and Simulation

M3MS-25IN0201032: Refine UO_2 Fuel Restructuring And Fragmentation In The Dark Zone For Application In Transient Fission Gas Release Simulations

Mesoscale Modeling for Restructuring and Fragmentation in High Burnup UO_2

SEPTEMBER 2025

Sudipta Biswas, Larry K. Aagesen, and Pierre-Clément Simon

Idaho National Laboratory

Xiaoyu Guan

University of Florida

Idaho National Laboratory

Battelle Energy Alliance manages INL for the U.S. Department of Energy's Office of Nuclear Energy

INL/RPT-25-88176
Revision 1

M3MS-25IN0201032: Refine UO_2 Fuel Restructuring And Fragmentation In The Dark Zone For Application In Transient Fission Gas Release Simulations

Mesoscale Modeling for Restructuring and Fragmentation in High Burnup UO_2

Sudipta Biswas, Larry K. Aagesen, and Pierre-Clément Simon
Idaho National Laboratory
Xiaoyu Guan
University of Florida

September 2025

Idaho National Laboratory
Computational Mechanics and Materials
Idaho Falls, Idaho 83415

http://www.inl.gov

Prepared for the
U.S. Department of Energy
Office of Nuclear Energy
Under DOE Idaho Operations Office
Contract DE-AC07-05ID14517

Page intentionally left blank

ABSTRACT

This report summarizes the mesoscale modeling conducted in Fiscal Year 2025 under the Nuclear Energy Advanced Modeling and Simulation (NEAMS) program, focusing on the microstructural evolution and restructuring in high burnup UO_2 nuclear fuel and its impact on fuel fragmentation. We developed a novel phase-field model to simulate restructuring behavior across different radial regions of high burnup fuel, including the dark zone and rim region. A grand-potential-based phase-field model is employed to concurrently evaluate subgrain formation and the growth of fission gas bubbles within the fuel. An energy-based subgrain formation criterion was introduced to simulate the restructuring process. The effects of temperature and burnup rate were studied to capture how each of these parameters influences the characteristics of the restructured fuel. Subgrain formation was observed to initiate around existing fission gas bubbles and proceed toward triple junctions, grain boundaries, and grain interiors. Under a given subgrain formation rate, the rate of restructuring increases with rising fuel temperature. The restructuring occurs faster with higher burnup rate. A restructuring bias was observed within the microstructure due to the variation in defect accumulation when comparing different grains. Microstructures corresponding to the dark zone and rim region can be obtained by parameterizing the model with the appropriate defect production rate, as determined based on the burnup rate and temperature. The predicted microstructures are consistent with experimental observations of the restructured regions. Based on the mesoscale simulations, a mechanistic model for restructuring and grain size evolution was implemented in BISON. Thus, this work provides a first-of-its-kind restructuring model for different regions of high burnup fuel for engineering-scale fuel performance analysis. It was shown that the model predicts appropriate grain size evolution along fuel radius as those observed in experiments. This model also enables BISON to calculate the effect of restructuring on fission gas release. Finally, phase-field fracture simulations with dark-zone-specific microstructures were performed to develop fragmentation criteria for the dark zone region. This work introduces a first-of-its-kind restructuring model for high burnup fuel, significantly enhancing BISON's predictive capabilities and expanding its applications for high burnup fuel analysis.

Page intentionally left blank

ACKNOWLEDGEMENT

This report has been funded by the Nuclear Energy Advanced Modeling and Simulations (NEAMS) program within the U.S. Department of Energy Office of Nuclear Energy. This report was authored by Battelle Energy Alliance, LLC, a contractor of the U.S. Government under contract DE-AC07-05ID14517. Accordingly, the U.S. Government retains a non-exclusive, royalty-free license to publish or reproduce the published form of this report, or allow others to do so, for U.S. Government purposes. This research made use of the resources of the High Performance Computing Center at Idaho National Laboratory, which is supported by the DOE Office of Nuclear Energy and the Nuclear Science User Facilities under contract no. DE-AC07-05ID14517.

This report was written with the assistance of AIVA (AI Virtual Assistant), a tool based on Large Language Models available at Idaho National Laboratory. The tools were used for checking spelling and grammar along with providing stylistic and structural suggestions.

Page intentionally left blank

CONTENTS

Page intentionally left blank

FIGURES

Page intentionally left blank

TABLES

Page intentionally left blank

ACRONYMS

BISON	MOOSE-based multidimensional fuel performance code
FFRD	fuel fragmentation, relocation, and dispersal
FGR	fission gas release
GBs	grain boundaries
HAGBs	high-angle grain boundaries
HBR	H. B. Robinson fuel
HBS	high burnup structure
HBu	high burnup
LAGBs	low-angle grain boundaries
LLS	lower length scale
LOCA	loss of coolant accident
LWR	light-water reactors
MOOSE	Multiphysics Object-Oriented Simulation Environment
NA	North Anna fuel
NEAMS	Nuclear Energy Advanced Modeling and Simulation
NRC	Nuclear Regulatory Commission
PBC	periodic boundary conditions
tFGR	transient fission gas release
UO_2	uranium di-oxide

Page intentionally left blank

M3MS-25IN0201032: Refine UO_2 fuel restructuring and fragmentation in the dark zone for application in transient fission gas release simulations

Mesoscale Modeling for Restructuring and Fragmentation in High Burnup UO_2

1. INTRODUCTION

In the United States, nuclear energy is crucial for supporting clean energy initiatives and meeting the nation's energy needs, providing nearly 20% of the total generated electricity in the country. Extended usage of light-water reactors (LWR) is necessary for improving the efficiency and economic advantages of the existing nuclear fleet. U.S. nuclear industries and the Nuclear Regulatory Commission (NRC) are currently considering the potential impact of increasing the burnup limit for LWR fuels to 85 MWd/kgU, which is well beyond the current regulatory limit of 62 MWd/kgU [8]. Extending this burnup limit could unlock several financial advantages, such as extended fuel cycle usages and reduced nuclear waste, both of which would have a positive effect on the environment. However, this increased fuel utilization entails significant design and material challenges, as well as safety risks [9].

At higher burnups, nuclear fuels undergo restructuring, leading to the formation of sub-micron grains and larger fission gas bubbles. The fuel's rim region, which is exposed to low temperatures and a level of local burnup 2–3 times higher than the average pellet burnup, exhibits a fine-grained microstructure with large micron-sized bubbles. This forms a defined rim around the periphery of the fuel pellet known as the high burnup structure (HBS) [10]. Furthermore, experimental observations of high burnup (HBu) revealed that restructuring occurs not only in the rim region, but also in another region closer to the fuel center [4, 5, 11]. This central region is sometimes referred to as the "dark zone" [1] (see Figure 1). Restructuring in HBu fuel has been correlated to diminished fuel performance, leading to accelerated fission gas release (FGR), as well as potential fuel fragmentation, relocation, and dispersal (FFRD) during loss of coolant accident (LOCA) [12]. This makes it crucial to understand the mechanisms behind the restructuring that occurs in different regions of the fuel, as well as its impact on the properties and performance of nuclear fuels.

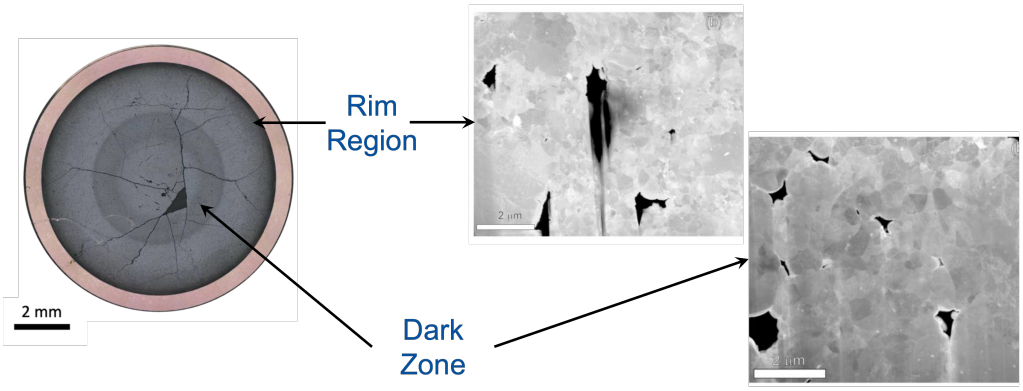

Figure 1. Different radial zones and corresponding restructured morphologies observed in North Anna fuel (NA). Reproduced from [1].

Restructuring in HBu fuel has primarily been studied experimentally by using advanced characterization techniques. Restructuring was first reported in the fuel's rim region, where large bubbles were surrounded by sub-micron grains, forming "cauliflower-like" structures [13]. Since that time, restructuring has been observed in various types of nuclear fuels, including ceramic- and metal-based fuels [11, 14–16]. Fuel samples have been irradiated at different burnups and temperatures to identify the threshold values beyond which restructuring occurs [17]. The key characteristics of HBu fuel are (1) the accumulation of dislocations and the creation of large dislocation networks, (2) the formation of new defect-free subgrains, (3) the depletion of intra-granular fission gas concentrations, and (4) the development of large spherical inter-granular bubbles. Among researchers, there is a lack of consensus regarding the mechanisms behind the restructuring observed in HBu fuel. Among the various proposed mechanisms are grain subdivision due to polygonization vs. recrystallization and continuous vs. discrete recrystallization, occurring either in tandem or in conjunction.

It is generally hypothesized that defect accumulation and dislocation interactions within the grains cause dislocation networks to be realigned into grain boundaries (GBs), leading to the formation of new subgrains that, over time, transform into new grains.

Because of the lack of transient data on how restructuring occurs, researchers have used advanced electron microscopy techniques to analyze the microstructure across the fuel radius. Studies of those irradiated samples with both partially and fully restructured regions are used to postulate the possible restructuring stages and governing mechanisms. Cappia et al. [18] analyzed a HBu specimen and identified three different regions across the fuel radius, each reflecting a different level of damage and restructuring as follows: a central area until $r/R \approx 0.55$, characterized by grain subdivision; an intermediate region from $r/R \approx 0.55$ until $r/R \approx 0.75 - 0.80$, with no restructuring and a lower porosity than the central area; and the rim region, featuring the rapid increase of porosity and the reduced grain sizes typical of HBS formation. Extension of restructuring beyond the rim region, along with sharp transitions between the different regions, has been reported by several researchers [1, 4, 11]. Moreover, both low-angle grain boundaries (LAGBs) and high-angle grain boundaries (HAGBs) were observed in various fractions at different radial locations in the HBu fuel. The dark zone shows a higher fraction of LAGBs in comparison to the fully restructured rim region [4]. Localized burnup, temperature, and stress are among the factors believed to govern the restructured fuel's characteristics in different regions.

Based on experimental observations, various empirical models were developed to capture the restructuring behavior in HBu fuel. Kinoshita [19] used a reaction-diffusion process model for calculating defects as a function of irradiation, and concluded that restructuring begins as a result of a self-organizing process that stems from dislocation network interactions with vacancies and interstitials. Rest [20] developed a model of the initiation and progression of restructuring as a function of fission rate, fission density, temperature, and initial grain size. This work provided threshold values for dislocation density, fission density, and bubble size distribution, thus identifying the onset of restructuring. Pizzocri et al. [21] proposed a semi-empirical model for grain size reduction due to the polygonization/recrystallization process. Barani et al. [22] analyzed various microstructural images obtained from experiments so as to compute the volume fraction of the restructured fuel as a function of effective local burnup. However, their model is based on very limited experimental data and does not account for the effect of temperature on restructuring. Moreover, these analytical models are limited to the conditions for which they were developed and mostly focus on the restructuring that occurs in the rim region. No existing model captures the restructuring observed in the dark zone. Furthermore, these models fail to account for the variabilities seen in grain morphologies and the spatial distributions of defects. Therefore, in this work, we aim to provide a more mechanism-informed restructuring model for high burnup uranium di-oxide (UO_2) and evaluate its impact on fuel fragmentation.

This report documents the advancements in the lower length scale (LLS) modeling of the restructuring behavior and associated fragmentation in HBu UO_2 fuel, done under the Nuclear Energy Advanced Modeling and Simulation (NEAMS) program. In Fiscal Year (FY) 2024, a restructuring model was developed for the dark zone of the HBu fuel. This year the model has been extended to other regions, including the rim region. To this end, we simulated restructuring at various temperatures and burnup rates. Based on the mesoscale simulations, a mechanistic model for restructuring has been developed and implemented in MOOSE-based multidimensional fuel performance code (BISON). By combining the evolution of restructuring volume fraction and average diameter of the new grains, the model appropriately captures the grain size evolution in HBu fuel across different radial locations. We also investigated an existing dislocation density evolution model from literature and identified additional development needs for improving the restructuring model. Finally, phase-field fracture simulations with dark-zone-specific microstructures were performed to determine the fragmentation criteria for the dark zone. This work introduces a pioneering mechanistic model for restructuring and fragmentation in HBu fuel that can be applied using BISON.

2. RESTRUCTURING IN HIGH BURNUP FUEL

The goal of this work is to provide a mechanistic restructuring model based on mesoscale simulations. At the mesoscale, we employed a phase-field model to capture the microstructural evolution in high burnup fuel. A grand-potential-based phase-field model was developed in FY 2024 to evaluate restructuring via subgrain formation. An energy-based subgrain formation criterion was introduced to simulate the restructuring process. The model also accounts for existing fission gas bubbles and concurrently tracks the concentration of defects (e.g., vacancies and gas atoms) that lead to further bubble growth. Last year, the work primarily focused on capturing the restructuring in the dark zone of the high burnup fuel. This year, the model has been extended to simulate restructuring at other radial locations, with an objective to explore the possibility of extending the model to the rim region. The effects of restructuring parameters, temperatures, and fission rate were evaluated to elucidate different restructuring scenarios and their impact on grain morphologies. The developed model can realistically simulate the restructuring behavior observed in different regions of high burnup fuel and can generate realistic microstructures similar to the ones observed experimentally. The details about the phase-field model can be found in References [23, 24]. Here we only present the restructuring criteria as relevant for the development of the mechanistic model in BISON. We also present and discuss the relevant results from the mesoscale simulations.

2.1. Mesoscale Restructuring Model

In the phase-field model, the restructuring of the grains is modeled as subgrain formation via dynamic recrystallization using a discrete nucleation algorithm. A energy balance-based criteria is introduced following the work proposed by Takaki et al. [25]. In this case, we assume that restructuring occurs when the dislocation energy is higher than the energy penalty for forming a new subgrain. Here, the dislocation energy density, f_d, is defined as

$$f_d = \frac{1}{2}\, G\, b_g^2\, d_{eff}\,. \tag{1}$$

where G is the shear modulus of the material, b_g is the Burgers vector, and d_{eff} is the effective dislocation density [26]. The dislocation density (d_i) within a grain is determined by following an empirical correlation fit to experimental observations [6, 27] such that

$$\log_{10} d_i = 2.2 \times 10^{-2}\beta + 13.8, \tag{2}$$

where β is the burnup in GWd/tU. Note that this correlates the pellet average burnup to the dislocation densities. We use the same correlation to calculate the dislocation density in the dark zone by substituting average burnup with local effective burnup. Here, the local effective burnup (β_{eff}) is defined as

$$\beta_{eff} = k_\beta\,(t - t_0)\ , \tag{3}$$

where k_β is the burnup rate in GWd/tU/s, t is current time, and t_0 is the initial time when a grain or subgrain is formed. Considering that dislocation densities within a grain can vary depending on its crystallographic orientation, the initial dislocation densities (d_{i0}) within different grains are assigned randomly such that

$$d_{i0} = R\, d_0\,, \tag{4}$$

where R is a random value in [0, 1] and d_0 is the specified constant dislocation density. The effective dislocation density is calculated as

$$d_{eff} = \frac{\sum_{i=1}^{n_m} d_i \eta_{mi}^2}{\sum_{i=1}^{n_m} \eta_{mi}^2}\,, \tag{5}$$

where d_i is the dislocation density within a grain. When a new subgrain is formed, the dislocation density within that subgrain is set to a lower value of 1×10^{-5} nm/nm^3, assuming that subgrain formation occurs due to the organization of dislocations into grain boundaries surrounding the nano-scale regions of defect-free material. This value is set such that it is below the dislocation density value at zero burnup according to Equation 2.

The subgrain formation energy is defined as

$$E_{sub} = k_s \gamma / D, \tag{6}$$

where γ is the interface energy (considered to be the same as the GB energy), D is the subgrain diameter, and k_s is a dimensionless geometrical factor for subgrain formation. Restructuring occurs via formation of new subgrains, when $f_d > E_{sub}$. The value of k_s in Equation 6 is set such that the subgrain formation based on the energy-based restructuring criteria begins at a threshold burnup consistent with experimental observations. Figure 2 shows the evolution of dislocation density and corresponding energy density with burnup. Subgrain formation energy for a 200 nm radius subgrain is overlaid to demonstrate the energy-based restructuring criteria. Assuming a subgrain radius of 200 nm and setting $k_s = 1.0$, the restructuring would begin above threshold burnup of 40 GWd/tU. This matches the experimental observations [4].

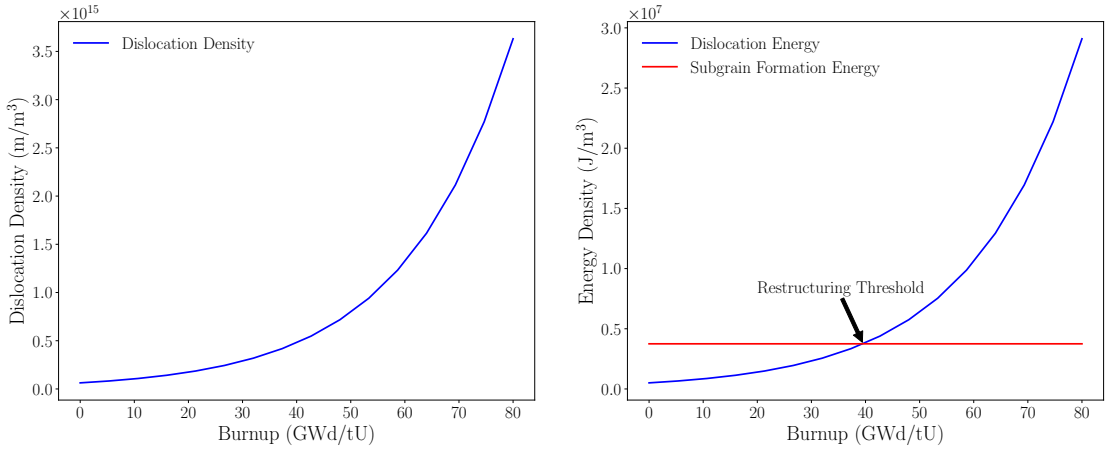

(a) (b)

Figure 2. Evolution of (a) dislocation density (Equation 2) and (b) dislocation energy density (Equation 1) within the fuel as a function of burnup. The subgrain formation energy is overlaid to demonstrate the restructuring threshold.

The new subgrains are introduced utilizing a discrete nucleation method where nuclei of a finite size are introduced in a stochastic fashion once the energy-based restructuring criteria is met. A simple linear relationship is employed to define the subgrain formation rate, $\dot{n}$,

$$\dot{n} = \langle \eta_i \eta_j \rangle \, k_d d_{eff}, \tag{7}$$

where k_d is the nucleation rate prefactor, indicating the fraction of the local dislocation density that contributes to the subgrain formation. Here, the function $\langle \eta_i \eta_j \rangle$ is defined as

$$\langle \eta_i \eta_j \rangle = 1, \text{ for } \eta_i \eta_j > \eta_{crit} \tag{8}$$

$$= 0, \text{ otherwise.} \tag{9}$$

The value for η_{crit} is considered to be 0.75. The term $\langle \eta_i \eta_j \rangle$ ensures that the new subgrains are formed around the grain boundaries of the existing grains and bubble surfaces. Furthermore, a nucleation bias is included for the bubble surfaces. Considering bubbles provide a free surface as a sink for dislocations, the energy penalty for creating a subgrain around bubble is reduced. Depending on the subgrain shape, the bubble surface covers a fraction of the subgrain boundary. Assuming only one segment of the subgrain boundary coincides with the bubble surfaces, the coverage fraction could be $1/6$ for a hexagonal grain. Whereas, for a circular grain the coverage fraction could be as high has $1/2$. For any other arbitrary grain shapes, the coverage fraction could vary. Based on this, the geometric factor for the subgrain energy in Equation 6 is modified such that

$$k_s = r_b k_{s0}, \text{for } \eta_b > 0.01 \tag{10}$$

$$= k_{s0}, \text{otherwise.} \tag{11}$$

We set $k_{s0} = 1.0$ and $r_b = 0.5$ to evaluate the effect of this local reduction in E_{sub} on the nucleation probability and restructuring fraction. The local nucleation probability, $P(r)$, is defined as

$$P(r) = v\,\dot{n}, \tag{12}$$

where v is the volume over which the local subgrain formation rate is being integrated. A Bernoulli trial is performed to determine whether a nucleus is introduced by comparing a random value R in [0, 1] against P. If $R < P$, a nucleus is introduced at that location.

2.2. Mesoscale Simulation Setup

A simulation domain of size $12.5\ \mu m \times 12.5\ \mu m$ was initialized with four grains. The average grain diameter at the beginning of the simulation was 7 μm, based on the grain size of the fresh UO_2. Dislocation densities within the grain are considered to be a function of grain orientation such that the initial dislocation densities vary from grain to grain. We start the simulations assuming that the initial grains were somewhat damaged and had accumulated a certain amount of dislocations. We initialize the dislocation densities within the grains ensuring that the maximum dislocation density of 6×10^{-4} nm/nm^3 is achieved in one of the grains. This assigns the initial dislocation densities within the grains slightly below the threshold value for restructuring, representing an initial burnup around 44 GWd/tU.

At the mesoscale, the simulation conditions are chosen based on experimental observations. Figure 3 shows the burnup and temperature profile in the radial direction of the fuel. The temperature range for the dark zone in H. B. Robinson (H. B. Robinson fuel (HBR)) fuel is around $r/R \approx 0.4 - 0.45$, corresponding to temperatures 1040 K to 998 K. For the rim region beyond $r/R \approx 0.93$, temperature is below 723 K (up to 650 K). For the North Anna fuel, the dark zone is around $r/R \approx 0.52 - 0.57$, corresponding temperatures are 1147 K to 1120 K. The rim is beyond $r/R \approx 0.9$, with corresponding temperatures 822 K to 700 K. It is also observable that burnup increases quickly in the rim region due to higher fission rate in the region. Based on this, various mesoscale simulations were performed with varying temperature, subgrain formation rate, and burnup rate to obtain the mechanistic restructuring model for BISON.

2.3. Mesoscale Simulation Results

To evaluate the effect of temperature on the restructuring and grain morphologies at different radial locations, mesoscale simulations were performed at 850 K, 900 K, 1000 K, 1050 K, 1100 K, and 1150 K temperatures. The burnup rate is considered 4.3×10^{-7} GWd/tU/s, corresponding to a fission rate of 1.09×10^{19} fission/m^3/s. The initial subgrain formation rate is considered as 5.3×10^{-5}. Ideally, the subgrain formation rates could vary with temperature. However, we kept them constant so as to enable an analogous comparison here.

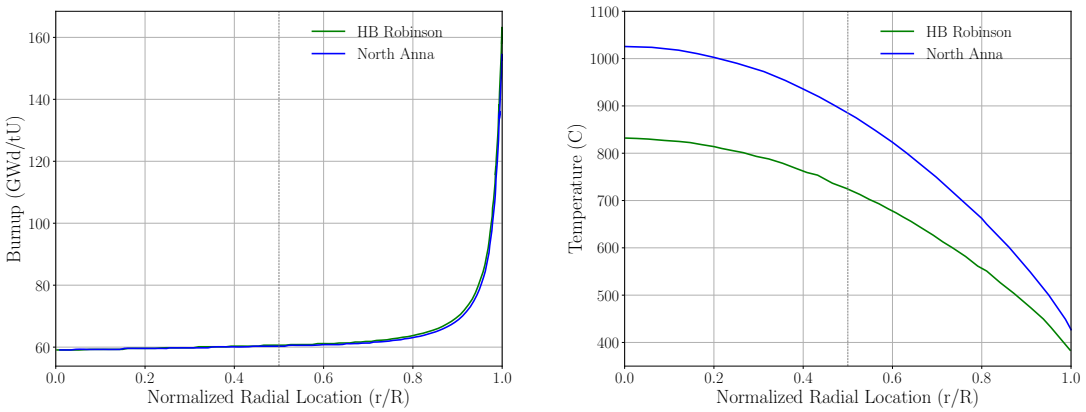

(a) (b)

Figure 3. Comparison of fuel burnup and temperature variations across radial direction at the end of life from simulated commercial pressurized water reactors (reproduced from [2] using Plotdigitizer [3]).

Different restructuring stages for 900 K and 1100 K temperatures are presented in Figure 4 and Figure 5, respectively, while Figure 6 compares the final grain morphologies corresponding to different temperatures. Restructuring is observed to occur in two stages: formation of new subgrains, followed by the coarsening thereof. Higher temperatures facilitate defect annihilation and subgrain coarsening, leading to faster restructuring. Generally, subgrain size increases with increasing temperatures due to the interplay of the competing phenomena of defect accumulation from irradiation and thermal annealing. At 900 K, more subgrains form with less coarsening, resulting in a lower average grain size. Consequently, both the rate of restructuring and average grain size increase with temperature, with restructuring occurring faster and average grain diameter becoming larger at higher temperatures. We also see that more bubble growth occurs at 900 K in comparison to at higher temperatures. At lower temperatures, the irradiation-enhanced vacancy diffusivity is relatively higher in comparison to the gas atoms. Furthermore, the presence of a denser GB network promotes vacancy diffusion, leading to the formation of new bubbles and the growth of existing ones. This will also be further investigated at a future time.

Additionally, the rim region experiences 2–3 times higher burnup than the average fuel pellet burnup. Hence, we simulated additional restructuring scenarios with different burnup rates, featuring the same initial subgrain formation rate. The mesoscale simulations are run with 4.3×10^{-7}, 1.3×10^{-6}, 4.3×10^{-6} GWd/tU/s burnup rates at 1000 K temperature. The initial subgrain formation rate was considered to be 6.2×10^{-6} in this case. A lower initial subgrain formation rate is used in this case to isolate the effect of burnup rate on restructuring and allow for the subgrain formation rate to grow significantly during the course of the simulations. Figure 7 compares the final grain morphologies obtained from the simulations with different burnup rates. It is observed that the restructuring happens faster with increasing burnup rate. It is also noteworthy that a higher burnup rate can induce multiple restructuring stages within the microstructure, due to continuous dislocation accumulation.

Figure 8 compares the evolution of the number of grains and average grain diameter with time at different temperatures, with an initial subgrain formation rate of 5.3×10^{-5}. Here, the average grain diameter (d_{avg}) is calculated by a circular grain approximation in 2-D such that $d_{avg}=2\sqrt{(A-A_{bub})/\pi N_{grain}}$, where A is the area of the simulation domain, A_{bub} is the area covered by the bubbles, and N_{grain} is the total number of grains. It is observed that the number of grains increases and the average grain diameter decreases during the subgrain formation stage. During the coarsening stage that then follows, the number of grain decreases and

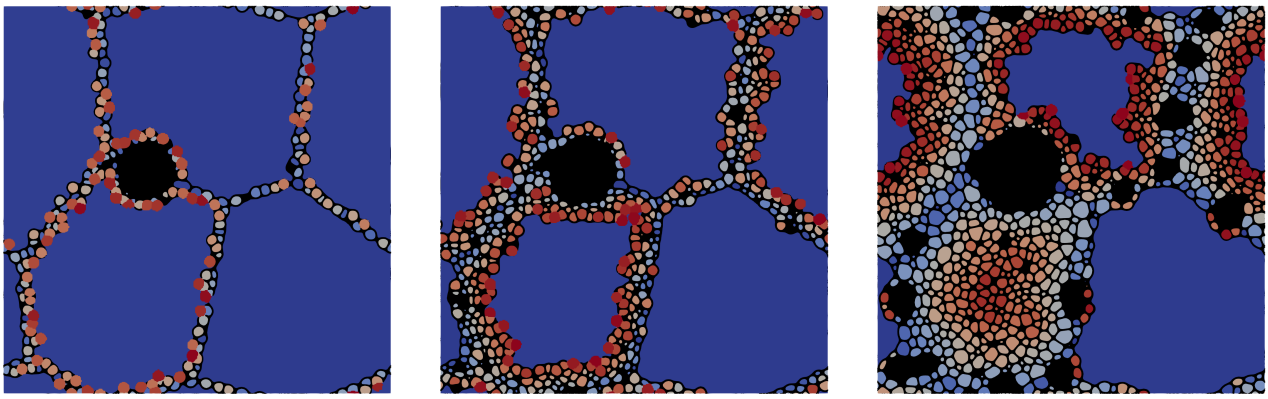

(a) (b) (c)

Figure 4. Different restructuring stages simulated at 900 K temperature at (a) 5.63×10^6 seconds, (b) 2.2×10^7 seconds, and (c) 1.0×10^8 seconds. The corresponding restructuring fractions are 16.3% at 46.9 GWd/tU, 31.62% at 53.8 GWd/tU, and 63.1% at 87.1 GWd/tU, respectively.

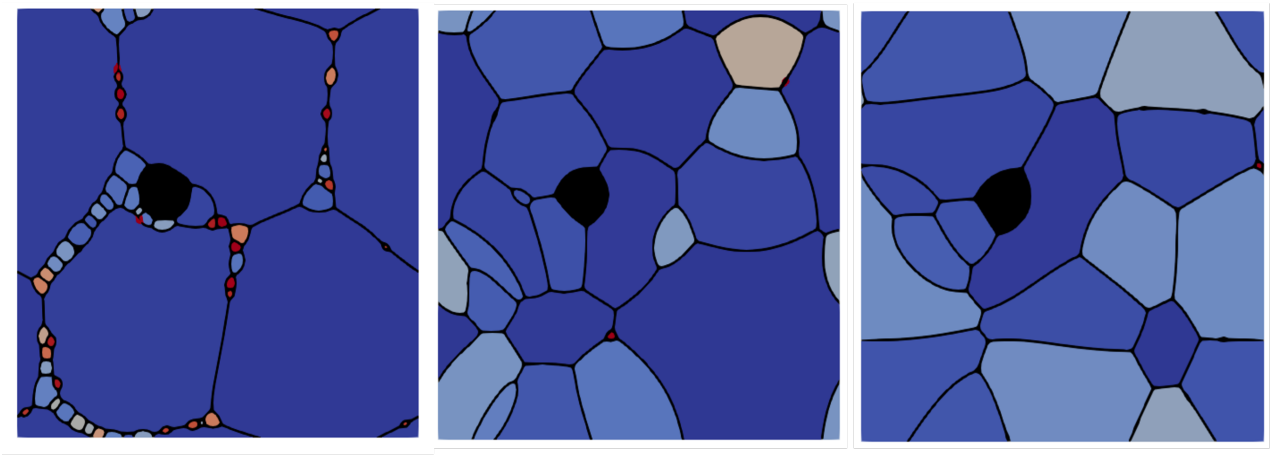

Figure 5. Different restructuring stages simulated at 1100 K temperature at 44.71 GWd/tU (left), 45.84 GWd/tU (middle) and 47.33 GWd/tU (right) burnup.

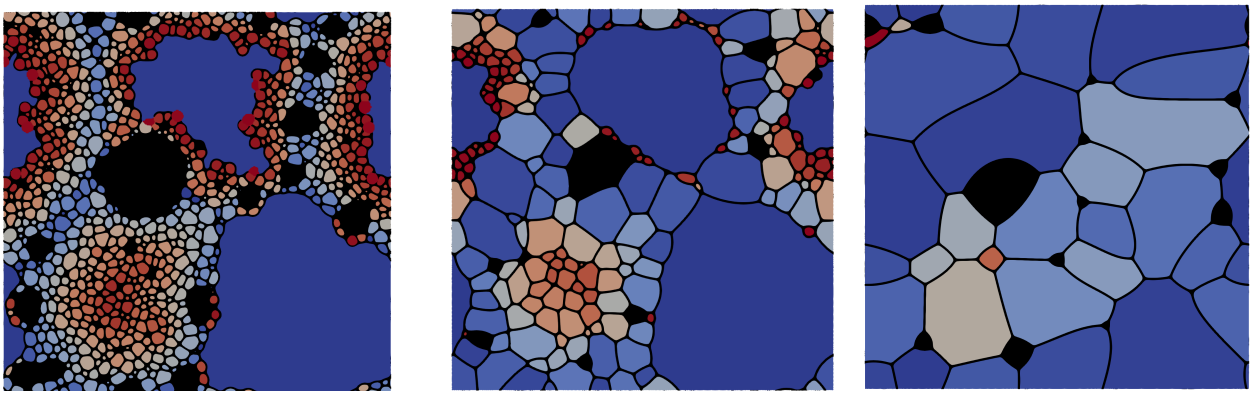

(a) (b) (c)

Figure 6. Restructured grain morphologies at (a) 900 K at 87.1 GWd/tU, (b) 1000 K at 58.6 GWd/tU and (c) 1050 K temperatures at 53.7 GWd/tU. The average grain sizes are 414 nm, 2 μm, and 3.9 μm, respectively.

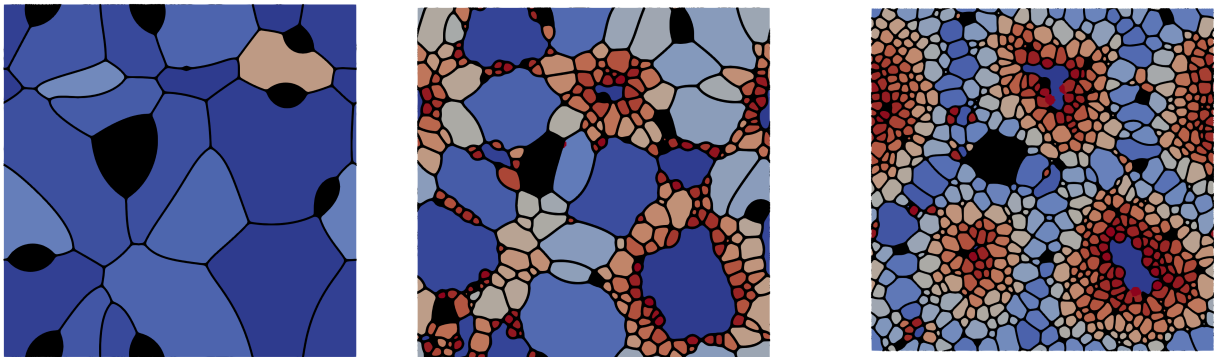

(a) (b) (c)

Figure 7. Restructured grain morphologies at 1000 K with burnup rates (a) 4.3×10^{-7} at 1×10^{8} sec (b) 1.3×10^{-6} at 7.74×10^{7} sec and (c) 4.3×10^{-6} GWd/tU/s at 2.92×10^{7} sec. The corresponding to a fission rates are 1.09×10^{19} fission/m^3/s, 3.27×10^{19} fission/m^3/s and 1.09×10^{20} fission/m^3/s, respectively.

the average grain diameter increases. Figure 9 compares the evolution of number of grains and average grain diameter with time for different burnup rates. In general, the number of subgrains increases and the average grain diameters decrease with a rising burnup rate. With higher burnup rate, dislocation density evolution happens faster, which results in higher subgrain formation rate. Therefore, more number of newer subgrains are formed and less coarsening is observed.

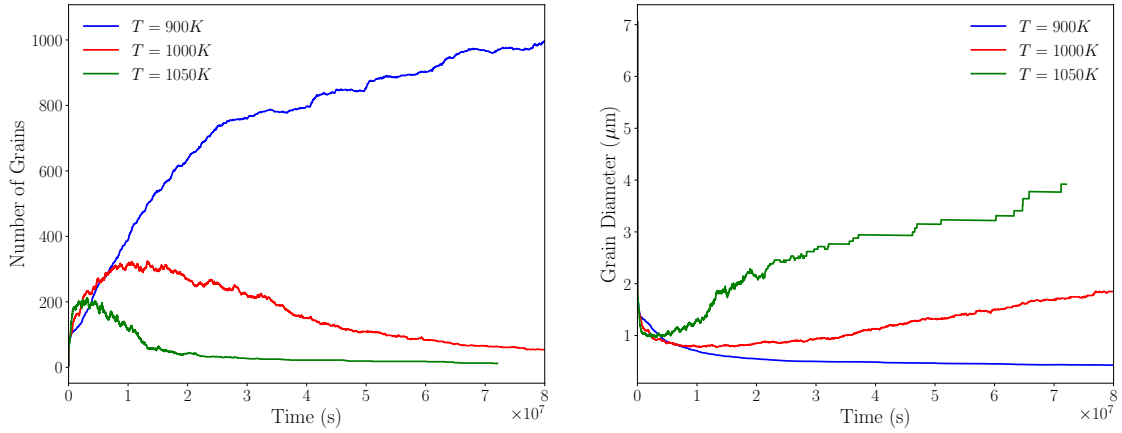

(a) (b)

Figure 8. Evolution of (a) number of grains and (b) average grain diameter with time for different temperatures, with an initial subgrain formation rate of 5.3×10^{-5}.

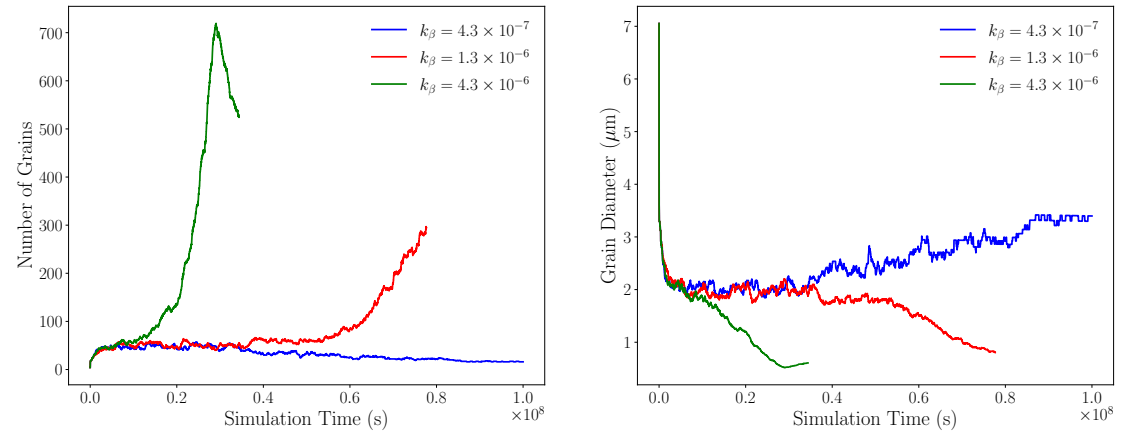

(a) (b)

Figure 9. Evolution of (a) number of grains and (b) average grain diameter with time for different burnup rates, with an initial subgrain formation rate of 6.2×10^{-6}.

2.4. Analysis Of Restructured Fuel Volume Fraction

By analyzing the outputs of the mesoscale simulations, we assimilate the combined effect of subgrain formation rate, burnup rate, and temperature on the restructuring behavior observed in high burnup fuel.

Figure 10 depicts the evolution of the volume fraction of restructured fuel as a function of local burnup for different temperatures. The restructured volume fraction is fitted using a modified Johnson-Mehl-Avrami-Kolmogorov (JMAK) correlation for phase transformations, similar to what was previously done in Reference [22] such that

$$\alpha = 1 - \exp\left[-k\ (\beta - \beta_{th})^{n}\right]\ , \tag{13}$$

where α is the volume fraction of the new subgrains, k is the transformation rate constant, n is the Avrami constant, β is the local burnup, and β_{th} is the threshold burnup value beyond which restructuring is observed. Based on the restructuring criterion described in Figure 16, the threshold burnup is taken as $\beta_{th} = 40$ GWd/tU. The fitting parameters corresponding to different combinations of subgrain formation rates, burnup rate, and temperatures are provided in Table 1. It also includes the average restructured grain size at the end of the simulation for each of the analyzed cases. In general, the rate of restructuring is observed to increase with a higher subgrain formation rate as well as temperature and burnup rate. Under a given subgrain formation rate, restructuring occurs faster at higher temperature, primarily due to the subgrain coarsening that occurs at higher temperatures. As observed in Figure 8, more subgrains are created at 900 and 1000 K than at 1050 K. However, higher temperatures allow for a greater amount of coarsening following the subgrain formation. Thus, the restructuring progresses faster at higher temperatures. With the increasing burnup rate, burnup accumulation happens faster within the same time, which results in accelerated defect generation and leads to faster restructuring. Figure 10b depicts the restructuring fraction evolution over time for different burnup rates. In this case, the higher burnup rates are representative of the rim region. Based on this analysis, a mechanistic restructuring model is developed for BISON (Section 2.6).

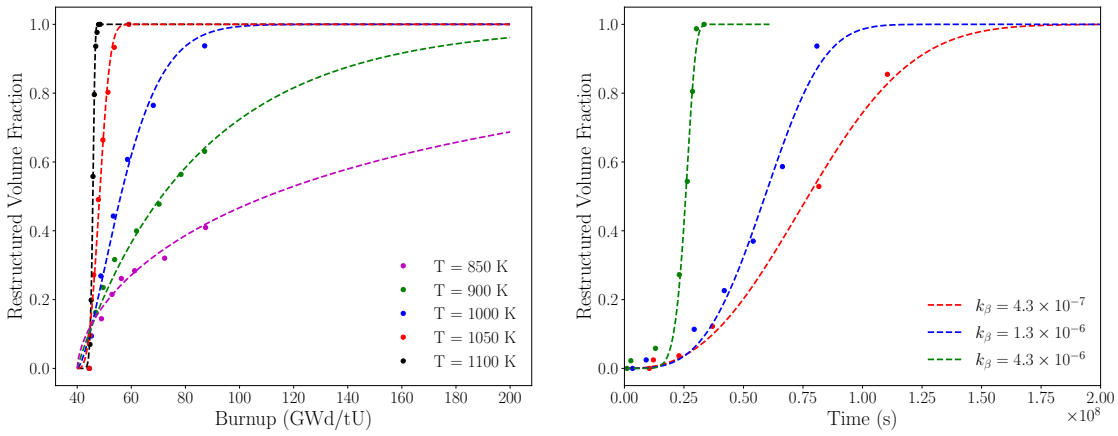

(a) (b)

Figure 10. Volume fraction of restructured fuel and the fitted JMAK relationship as a function of local burnup for (a) different temperatures and (b) different burnup rate at 1000 K temp. The corresponding fitting parameters are listed in Table 1.

Temperature (K)	Burnup Rate (GWd/tU/s)	Initial Subgrain Formation Rate ($\dot{n}$)	Transformation Rate Constant (k)	Avrami Constant (n)	Average Grain Diameter (μm)
850			4.85×10^{-2}	0.626	0.295
900			2.66×10^{-2}	0.95	0.320
1000			1.044×10^{-2}	1.51	1.987
1050	4.3×10^{-7}	5.3×10^{-5}	1.127×10^{-3}	3.04	3.92
1100			4.211×10^{-8}	9.47	3.912
1150			8.785×10^{-20}	27.68	3.912
	4.3×10^{-7}		8.152×10^{-5}	2.59	3.367
1000	1.3×10^{-6}	6.2×10^{-6}	2.273×10^{-7}	3.44	0.796
	4.3×10^{-6}		4.116×10^{-18}	8.44	0.615

Table 1. JMAK fitting parameters and average new grain diameter for the cases presented in Figure 10.

2.5. Comparison With Experimental Data

In this section, we compare the characteristics predicted by the mesoscale model presented in this work to experimental observations. Figure 11a through Figure 11d display sample microstructures from different radial locations in HBR [4] and NA [5]. Among these, Figure 11a and Figure 11b depict the central restructured zone, i.e., the dark zone, while Figure 11c and Figure 11d represent partially restructured regions closer to the rim. It is observed that restructuring initiates around the existing bubbles and then proceeds toward grain interiors. In addition, different regions within the same micrograph exhibit varying levels of restructuring. For example, Zone A and Zone B in Figure 11a illustrate the partially and fully restructured regions in the dark zone. This suggests that a restructuring bias exists, depending on the bubble distribution and the damage accumulation within the grains. The current model effectively captures all these phenomena. The simulations performed at 1000 K and higher temperature with low burnup rate are considered to be representative of the dark zone microstructures. On the other hand, simulations performed at 900 K and 850 K temperature, higher burnup rate and subgrain formation rate replicate the regions closer to the fuel rim. Qualitatively, the simulated microstructures show similar characteristics as those observed in these figures, indicating that the model appropriately represents the restructuring observed in high burnup fuel.

Figure 11e and Figure 11f present the grain size variation along the radial direction of the fuel, as observed in different restructured fuels [2]. The average grain diameter obtained from the mesoscale simulations corresponding to different temperatures are overlaid for comparison. For the HBR fuel, the sharp decrease in grain size is observed at a position around 0.4. According to Gerczak et al. [4], the central restructured zone is observed from radial locations 0.35 to 0.45, with temperatures between 1000 and 1050 K (see Figure 3). A significant decrease in average grain size is again evident in the rim region beyond $r/r_o \approx 0.8$, indicating transition to HBS. In the case of North Anna fuel, the grain size decreases radially in the central region, with a sharp decrease in grain size being observed at around radial position 0.55.

The radial locations for the mesoscale simulations are approximated based on the temperature profile from Figure 3. The average grain diameters reported in the dark zone are 3.6 and 6 μm for the HBR and NA, respectively [2]. Simulations representing the dark zone show average grain diameter ranging from 2 to 3.9 at the end of these simulations. The maximum simulated value closely aligns with the grain diameter observed in the dark zone of the HBR fuel [2, 4].

The average grain size in the rim region with fully formed HBS is reported to be around 600 nm for both these fuels. For the simulations representing regions close to the rim, the average grain diameter varies from

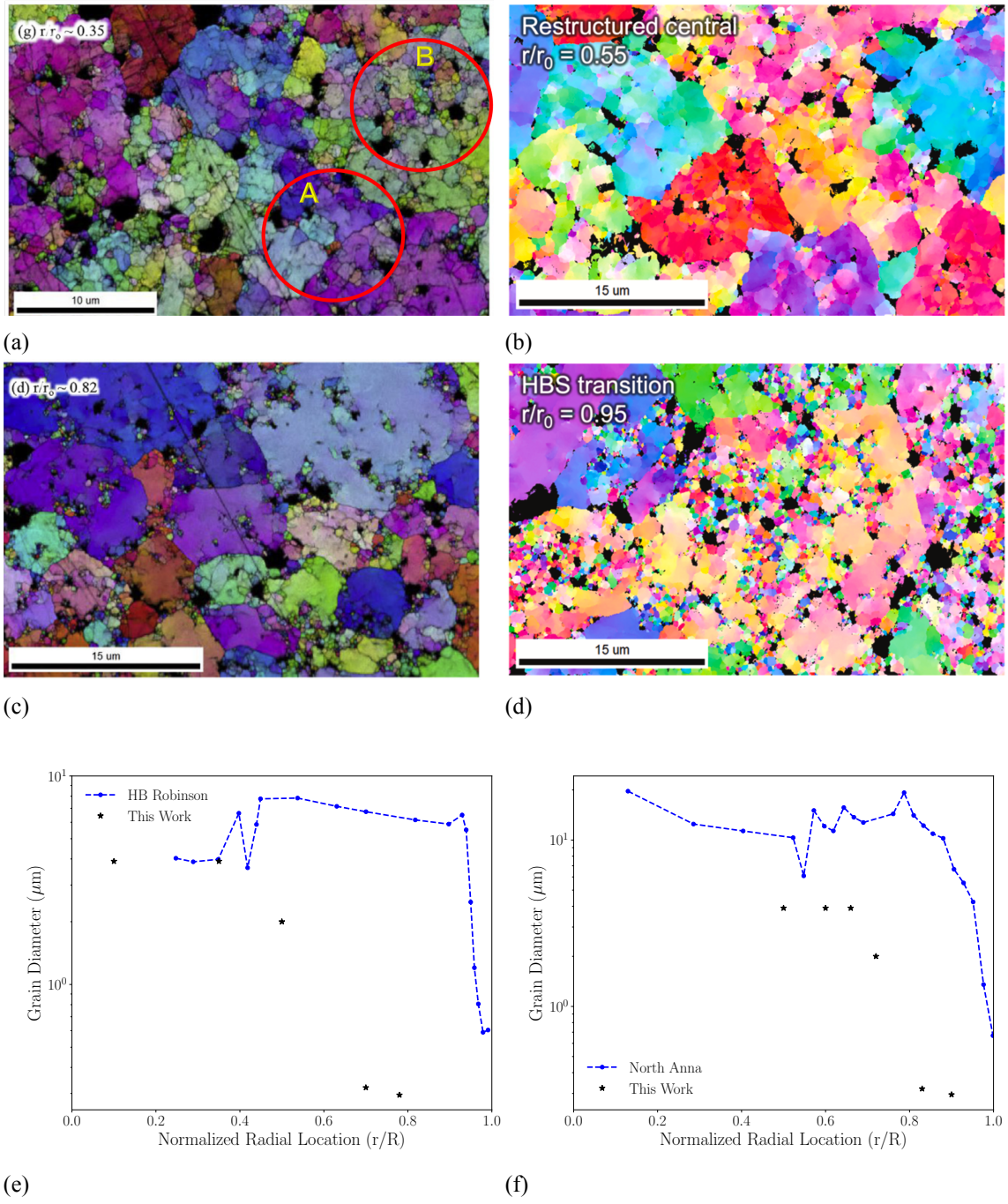

Figure 11. Microstructure observed in the HBR fuel at locations (a) $r/r_o \approx 0.35$ and (c) $r/r_o \approx 0.82$ [4]. Microstructure observed in the NA at locations (b) $r/r_o \approx 0.55$ and (d) ≈ 0.95 [5]. Comparison of average grain diameter obtained from the mesoscale simulations presented in this work with the grain size variations across the radial direction, as observed in (e) HBR and (f) NA (reproduced from [2] by using Plotdigitizer [3]).

400 nm to 930 nm, depending on the restructuring stages. It is noteworthy that the simulated grain sizes are significantly smaller compared to the North Anna data. This is primarily attributed to the difference in grain sizes prior to the onset of the restructuring. More rigorous statistical analysis in this regard will be pursued in the future.

2.6. Mechanistic Restructuring Model For BISON

Restructuring in the high burnup fuel has significant implications on the fuel performance, including fission gas release and fragmentation during normal operating and accident conditions. In order to evaluate the performance of the high burnup fuel, it is important to understand the mechanisms of restructuring and associated microstructural changes in the fuel. Therefore, we first compare the restructuring predicted by the mesoscale simulations with the existing BISON model for HBS [22, 28] (Figure 12). The existing BISON model relies on empirical fitting to a limited set of experimental data. It fails to account for temperature and fission rate dependence of the restructuring. Moreover, the model represents the restructuring fraction as a function of effective burnup, which is defined as a Heaviside function based on threshold temperature for restructuring observed in different radial locations. Thus, the fuel performance code BISON [29] lacks a unified restructuring model for the high burnup fuel. Hence, it fails to predict the grain size reductions observed in different radial locations in high burnup fuel. Updating this model is crucial for improving fuel performance predictions. The current work aims to provide a first-of-its-kind, mechanistic restructuring model to the fuel performance code BISON.

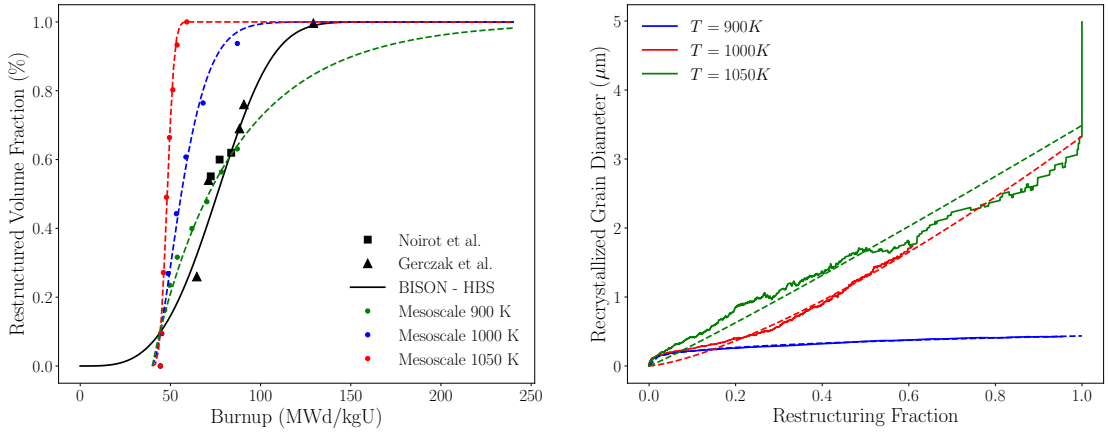

(a) (b)

Figure 12. (a) Comparison of the mesoscale predictions with the current BISON model and experimental data. (b) Variation in restructured grain size with restructuring fraction for different temperatures.

To this end, we fit the transformation rate constant k and Avrami constant n as a function of temperature (Figure 13) as follows

$$k = 1983.66 \exp\left(-0.0125T\right), \tag{14}$$

and

$$n = 9.19 \times 10^{-26} T^{8.44}. \tag{15}$$

Only part of the data set (below temperature 1100 K) was used in fitting n, since it is very sensitive to temperature at the lower temperature range. Additionally, the fission rate dependence is also implemented by

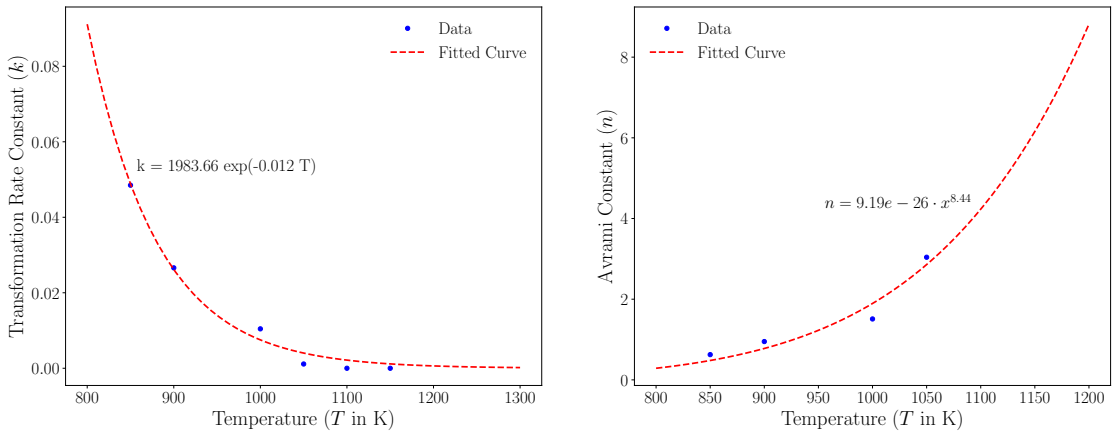

(a) (b)

Figure 13. Fitted correlation for the transformation rate constant and Avrami constant as a function of temperature using the data from Table 1.

accounting for the burnup-rate dependence on the restructuring model. Since burnup accumulation happens linearly given a specific burnup rate, we assume the same correlation for the restructuring fraction. Thus, the coefficients k and n are modified such that

$$k = 1983.66 \exp\left(-0.0125T\right)\frac{\beta}{\beta_0}, \tag{16}$$

and

$$n = 9.19 \times 10^{-26} T^{8.44}\frac{\beta}{\beta_0}, \tag{17}$$

where β is the local burnup and β_0 is the burnup at the fuel centerline. Thus, the term $\frac{\beta}{\beta_0}$ is equivalent to the radial peaking factor for fission rate. This enables capturing the effect of varying fission rate along fuel radius.

Furthermore, to obtain the average grain size of the restructured fuel, the new subgrain diameters were fitted as a function of restructuring fraction (Figure 12b) such that

$$d^m = s \cdot \alpha \tag{18}$$

where d is the diameter of the new subgrains in μm, α is the restructured volume fraction, m and s are the growth rate constant and power coefficients obtained from the fitting. Here, the average diameter (d_{new}) of the new grains is calculated as $d_{new} = 2\sqrt{\alpha(A - A_{bub})/\pi(N_{grain} - N_0)}$, where A is the area of the simulation domain, A_{bub} is the area covered by the bubbles, α is the restructuring fraction, N_{grain} is the total number of grains, and N_0 is the number of original grains. The fitting coefficients obtained for Equation 18 are provided in Table 2.

Temperature (K)	Growth Rate Constant (s)	Power Coefficient (m)
900	0.063	3.33
1000	2.4	0.73
1050	3.63	1.184
1100	4.738	1.2
1150	4.575	1.245

Table 2. Fitting parameters for the new grain size evolution with restructured volume fraction at different temperatures.

The fitted correlation for m and s as a function of temperature are

$$s = \frac{4.74}{1 + \exp\left[-0.03(T - T_0)\right]}, \tag{19}$$

and

$$m = 3.8 \times 10^{49} \exp(-0.126\, T) + 1.088. \tag{20}$$

Here, T_0, as obtained from the fitting, is 1002 K. As observed in Figure 12b, at higher temperatures, the new subgrains continue to grow even after 100% restructuring has occurred. Here, we ignore this for the fitting as the normal grain growth model should apply once the fuel is fully restructured.

This mechanistic restructuring model was implemented in BISON. For preliminary testing, we use a temperature profile fit using a polynomial correlation to the thermal profile of HBR fuel, as was done in Reference [28]. The corresponding burnup profile was implemented as a piecewise linear function. The variation of the restructuring fraction along fuel radius is shown in Figure 14a. We also compare the temperature-only model (Equation 14 and Equation 15) with the fission rate dependence model (Equation 16 and Equation 17). It is observed that the restructuring fraction reduces significantly after $r/R \approx 0.5$ and then increases again in the rim region, beyond $r/R \approx 0.8$, due to accelerated burnup. However, the model shows a gradual transition after the dark zone as compared to the sharp transition observed in experiments. Figure 14b provides the variation in the average diameter of the newly formed subgrain along the fuel radius, as obtained from Equation 18. The model predictions can be improved further in the future by implementing a more mechanistic dislocation density evolution model, as discussed in Section 3.

Furthermore, we calculate the average grain size variation along fuel radius, assuming an initial grain size of 20 μm prior to restructuring (Figure 15). The average grain diameter (d_{avg}) here is calculated as

$$d_{avg} = \alpha\, d_{new} + (1 - \alpha) d_0, \tag{21}$$

where d_{new} is the average diameter of the new grains, α is the restructured volume fraction, and d_0 is the average grain diameter at the onset of restructuring. This postulates that the rate of restructuring is invariant with respect to the initial grain size. We compare the prediction of this mechanistic model to the grain size variation measured in NA and HBR fuels [5]. As demonstrated in Figure 15b, the model appropriately captures the restructuring trend observed in HBu fuel. However, the actual grain size may differ from experiments due to the assumptions of initial grain/subgrain sizes, rate of restructuring, etc. The grain size prediction can be improved further when the restructuring model is used in combination with the mechanistic grain growth model for UO_2 such that the radial grain size variation prior to restructuring, as well as continued grain growth of the fully restructured fuel, is taken into account.

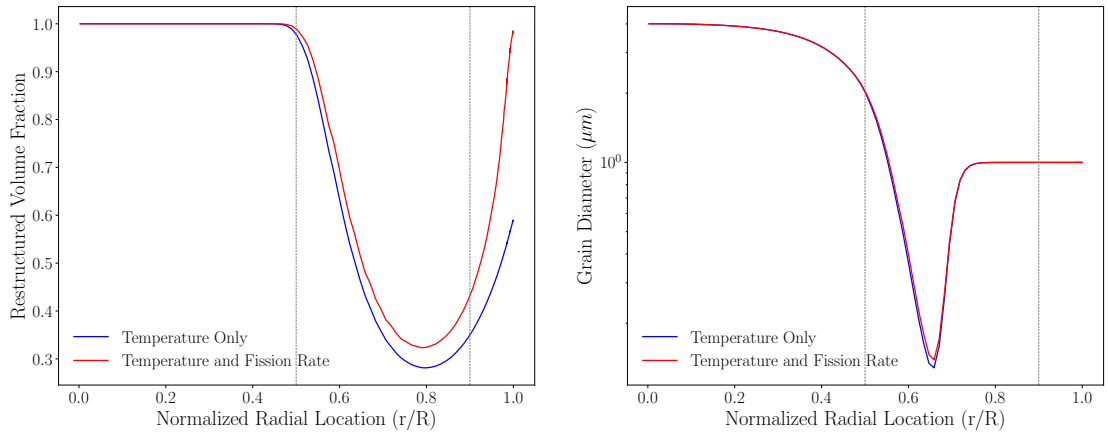

(a) (b)

Figure 14. Variation of the (a) restructuring fraction and (b) restructured grain size along fuel radius. The temperature-only model is compared with the fission rate dependence model.

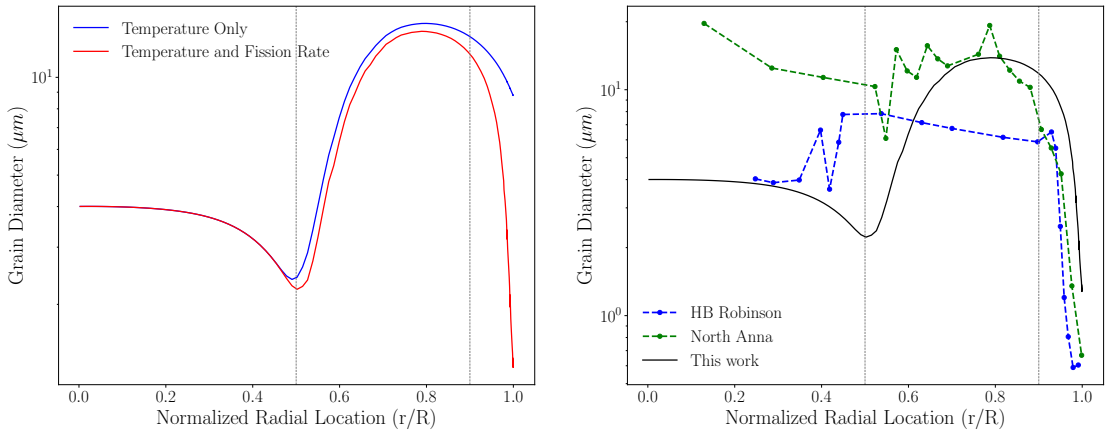

(a) (b)

Figure 15. Variation of average grain size along fuel radius: (a) comparison of the temperature-only model with the fission rate dependence model and (b) comparison with the experimental data.

3. DISLOCATION DENSITY EVOLUTION

As described in Section 2, the phase-field model currently makes use of an empirical equation for dislocation density, given in Equation 2. This equation was fit to experimental observations of dislocation density [6]. However, the experimental data used to develop the fitted model was obtained from experiments in a limited temperature range estimated as 630–750 °C and a range of linear heat generation rates ranging from 180–370 W/cm, which were not converted to equivalent fission rates. Thus, Equation 2 is only dependent on burnup and lacks dependence on temperature or fission rate.

To address this issue, in this section, an existing mechanistic model of dislocation density evolution from the literature [7] is evaluated. Our implementation is compared to the published results of the model, as well as the experimental data of Reference [6]. The model is studied parametrically to understand the effects of its parameters and provide guidance for future work.

3.1. Dislocation Evolution Model Formulation

In Reference [7], the time evolution of dislocation density ρ_N (in units of m/m^3) is given by

$$\frac{d\rho_N}{dt} = \pi v_1 n_1 - \frac{v_1 (f(v)/\pi)^{1/2}}{C_A C_\rho} \rho_N^{3/2} , \tag{22}$$

and

$$v_1 = \frac{2 Z_{iv}}{b_v} D_i c_i , \tag{23}$$

where n_1 is the interstitial loop density, v_1 is the interstitial loop climb-controlled glide velocity, $f(v) = (1-\nu/2)/(1-\nu)$, ν is Poisson's ratio, C_A and C_ρ are geometric factors with values of 3 and 1, respectively, Z_{iv} is the relative bias between interstitials and vacancies, D_i is the interstitial diffusivity, c_i is the interstitial concentration, and b_v is the Burgers vector for UO_2. In Equation 22, the first term represents dislocation line length creation due to the accumulation of interstitial loops, and the second term represents loss of line length due to self-annihilation of edge dislocations. The interstitial loop density n_1 is given by [7]

$$n_1 = \left[\frac{\sqrt{2} b_v}{4\pi Z_{iv} \Omega^{5/3}} c_i \rho_N \right]^{1/2} , \tag{24}$$

where Ω is the atomic volume. Combining Equations 22–24 and solving analytically allows for ρ_N to be solved as a function of time:

$$\rho_N(t) = \frac{c_1}{c_2} \left[\frac{1 - e^{\sqrt{c_1 c_2} t}}{1 + e^{\sqrt{c_1 c_2} t}} \right]^2 , \tag{25}$$

where

$$c_1 = \left[\pi v_1 \frac{\sqrt{2}}{2} D_i c_i^2 / \Omega^{5/3} \right]^{1/2} , \tag{26}$$

and

$$c_2 = \frac{v_1 (f(v)/\pi)^{1/2}}{C_A C_\rho} , \tag{27}$$

The steady-state concentration of interstitials, c_i, is taken from a simple rate theory approach neglecting the interstitial and vacancy sinks such that

$$c_i = \frac{1}{D_i} \left(\frac{\Omega D_v K}{4\pi r_{iv}} \right)^{1/2} , \tag{28}$$

Parameter	Value	Reference
D_i^0	5 m^2/s	[30]
D_v^0	75 m^2/s	[30]
ε_i	0.6 eV	[30]
ε_v	2.4 eV	[31]
r_{iv}	8.25 nm	[30]
Z_{iv}	5×10^{-4}	[30]
a	0.547 nm	[32]
b_v	$\sqrt{2}a/2$	[32]
$\dot{f}$	2×10^{19} m^{-3} s^{-1}	[7]
K	$\dot{f}/10^{23} = 2 \times 10^{-4}$ dpa/s	[7]
ν	0.345	[33]
Ω	$a^3/4$	[7]

Table 3. Parameters used for dislocation density evolution model as given in Reference [7].

where D_v is the vacancy diffusivity, K is the damage rate in dpa/s, and r_{iv} is the interstitial-vacancy recombination distance. The vacancy and interstitial diffusivities are given as

$$D_i = D_i^0 \exp\left(\frac{-\varepsilon_i}{kT}\right), \tag{29}$$

$$D_v = D_v^0 \exp\left(\frac{-\varepsilon_v}{kT}\right), \tag{30}$$

where D_i^0, D_v^0 are the prefactors and $\varepsilon_i, \varepsilon_v$ are the activation energies. The baseline values of the parameters used in the model are given in Table 3.

3.2. Dislocation Model Results

3.2.1. Evaluation of Model in Published Form

In Figure 16a, the evolution of ρ_N from the mechanistic model of Equations 25–27 as published in Reference [7] is compared to the data of Reference [6] and to the model of Equation 2. The mechanistic model under-predicts the experimental data by an order of magnitude at lower burnups, but accurately predicts ρ_N the highest burnup of 83 GWd/tU.

To assess the model further, Equations 25–27 were implemented in a Python script. For verification, our implementation for 953 K was compared to the plot provided in the paper. As shown in Figure 16b, our implementation gives different results from what was reported in the paper. To ensure the differences were not due to an error in our implementation, an independent author of this report implemented the model of Equations 25–27, and the same results were obtained as the first author of this report. Thus, it is believed that an error exists in the published data of Reference [7], in either the implementation or parameters used. Our implementation shows that the predicted ρ_N saturates at approximately 3.6×10^{13} m/m^3, significantly lower than the experimentally reported value of 6.0×10^{14} m/m^3.

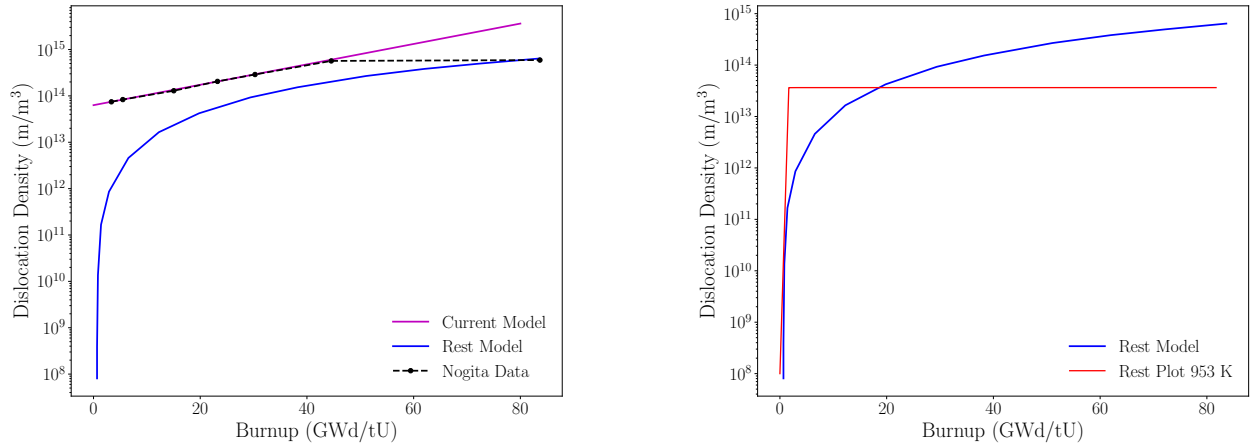

(a) (b)

Figure 16. (a) Comparison of experimentally measured dislocation density data from Nogita [6] with current model of Equation 2 and published results of the Rest model [7]. (b) Comparison of the Rest model output as published in [7] with our implementation at 953 K (Rest Plot 953 K).

3.2.2. Parametric Study of Model Performance and Fit to Match Published Model Results

Since the model of Equations 25–27 does not match the experimental data well, potential causes of the discrepancy were investigated. The model relies on a large number of parameters, as seen in Table 3. To identify potential causes of the discrepancy, a parametric study was performed to find which parameters most significantly influence the model results and to determine which parameters give a better match to the plot presented in the paper. For this analysis, the initial dislocation density of the grains were considered to be 1×10^8 m/m^3.

The damage rate K was varied from its initial choice of 2×10^{-4} dpa/s in Figure 17a. Decreasing values of K result in a lower saturation value of the dislocation density, and a higher burnup is required to reach the saturation value. This is due to the slower buildup of dislocations since they are not created from interstitials as rapidly due to the lower damage rate and corresponding lower interstitial concentration.

The effects of ε_v and ε_i are shown in Figures 17b and 17c, respectively, beginning from their baseline values of 2.4 eV and 0.6 eV. Decreases in ε_v result in a lower value of D_v, and by Equation 28, give a higher value for interstitial concentration, resulting in a larger saturation value of ρ_N with a more rapid approach to that value. The changes to ε_i are more complicated to interpret physically since the interstitial diffusivity enters into the governing equations in multiple places.

The effect of the interstitial absorption bias Z_{iv} is shown in Figure 17d. Decreases in Z_{iv} result in a slower approach to steady-state defect concentration. The physical cause of this change is difficult to interpret, since Z_{iv} appears in both the prefactors to the generation and annihilation terms of Equation 22 through the factor of v_1, as well as through the interstitial loop density n_1.

Guided by this parametric study, a set of parameters that reasonably matched the published data of the model [7] was determined, as shown in Figure 18a. The model with $Z_{iv} = 5 \times 10^{-6}$ and $\epsilon_i = 1.0$ eV provided the best match to the published data. Using the model with these parameters, and the remaining as given in Table 3, the effect of temperature was considered, with the results shown in Figure 18b. At higher temperatures, a higher saturation value of ρ_N is reached, with lower burnup needed to obtain that saturation

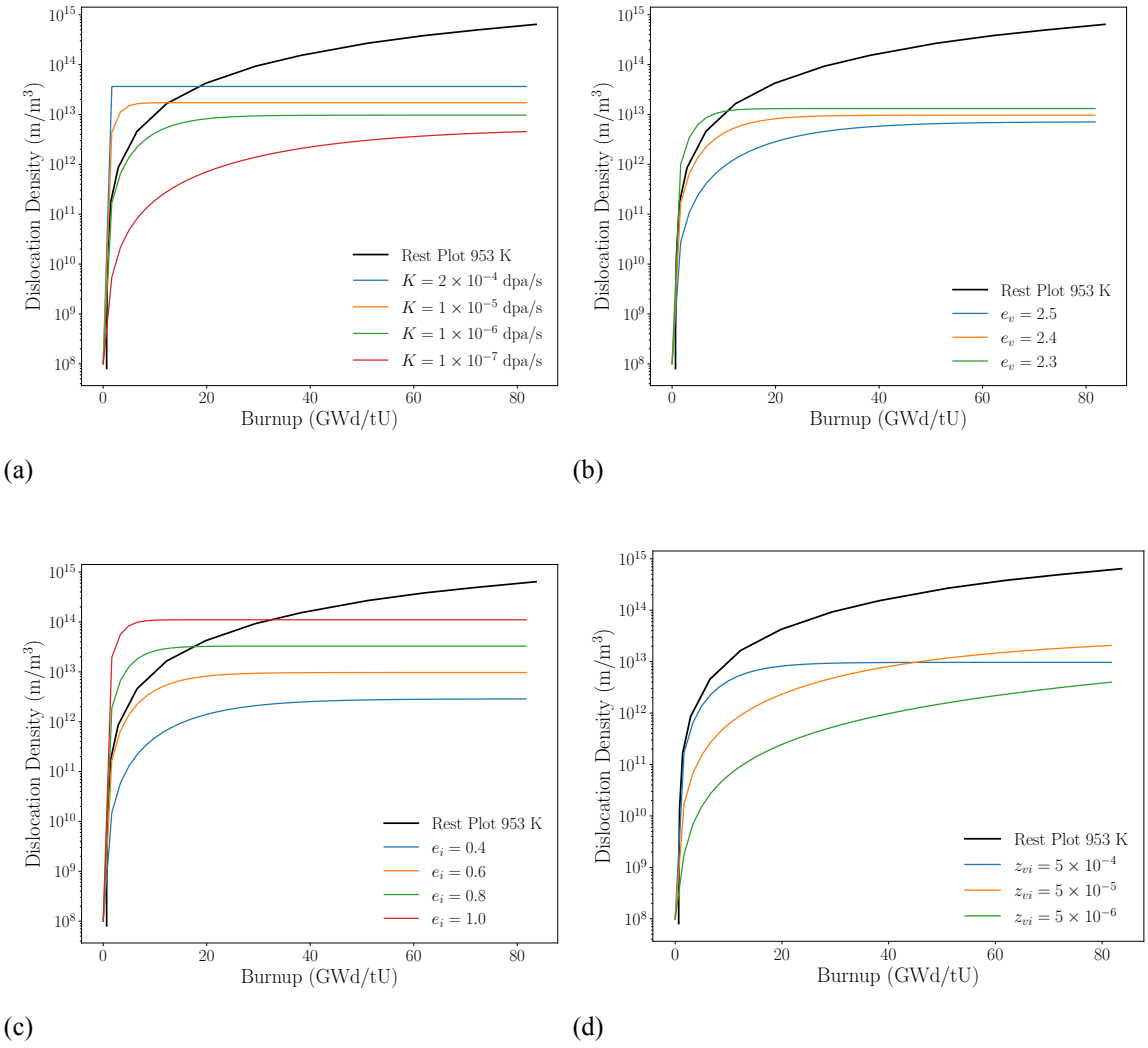

Figure 17. Parametric study to evaluate the effect of model parameters on the dislocation evolution at 953 K. Comparison with Rest plot for 953 K provided in [7]. Dose rate of $K = 1 \times 10^{-6}$ dpa was used for Figures (b) to (d).

value.

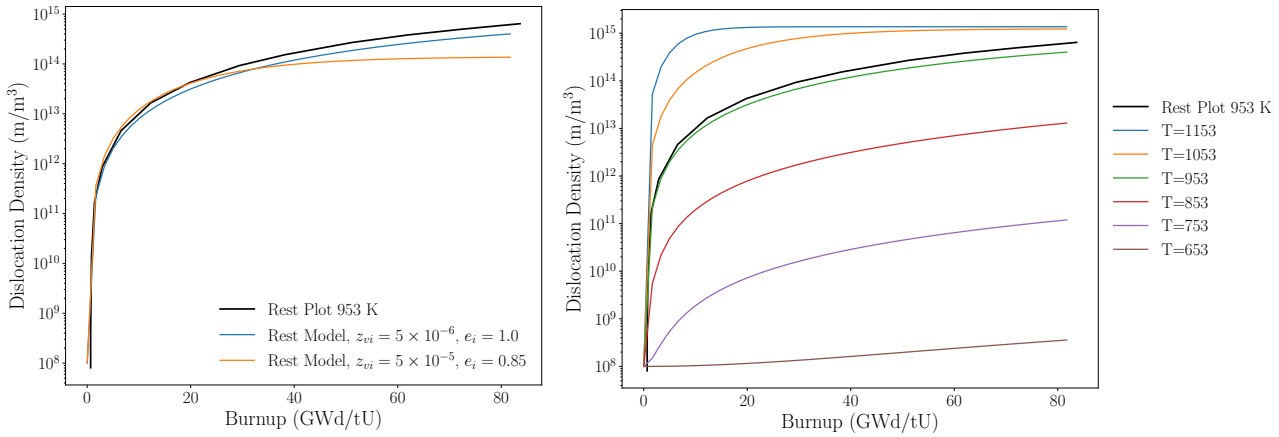

(a) (b)

Figure 18. (a) Choice of parameters to obtain a better match with the 953 K plot provided in Reference [7]. (b) Effect of temperature captured with the finalized model.

Although the lack of agreement between the model and the experimental data shown in Figure 16a precludes its use in the current form, it can provide some qualitative explanation of trends observed in some high burnup fuel. The temperature and local burnup, as a function of radius for the North Anna [5] and H. R. Robinson [4] high burnup fuel samples, were calculated using the BISON fuel performance code [2], with the results reproduced in Figure 19a. The dislocation density calculated using the model of Reference [7] (with $Z_{iv} = 5 \times 10^{-6}$ and $\epsilon_i = 1.0$ eV) for these two cases is shown in Figure 19b. The model predicts that the higher temperature of the North Anna fuel results in a higher dislocation density for a given value of r/R. Figure 19b also suggests that if a constant threshold dislocation density must be reached to allow the onset of restructuring (leading to the formation of the dark zone), it would occur at a larger value of r/R for the North Anna fuel than for the H. B. Robinson fuel. This is consistent with experiments, where it was observed that significant restructuring (based on a significant drop in measured grain size) begins in the North Anna fuel at $r/R \approx 0.58$ [5], whereas in the H. B. Robinson fuel, restructuring begin at $r/R \approx 0.45$ [4].

However, much work remains to bring the dislocation density model in quantitative agreement with experiments. As seen in Figure 16a, the model does not agree particularly well with the data from Reference [6]. The model also does not predict a significant increase in dislocation density in the rim region, as seen in Figure 19b. Assuming that rim region restructuring is driven by dislocation density accumulation and subsequent polygonization, an increase in dislocation density would be needed to account for rim region restructuring.

3.2.3. Evaluation of Dislocation Evolution Model with Updated Parameters from the Literature

Since the time that Reference [7] was published, updated values have become available for some parameters used in the model. The parameters were updated to determine whether they resulted in improved agreement with experiment. The parameters D_i^0, D_v^0, ε_i, ε_v, r_{iv}, and K were updated as follows. Interstitial diffusivity was assumed to be dominated by the defect complex $U_i 2O_i$, whose activation energy was calculated

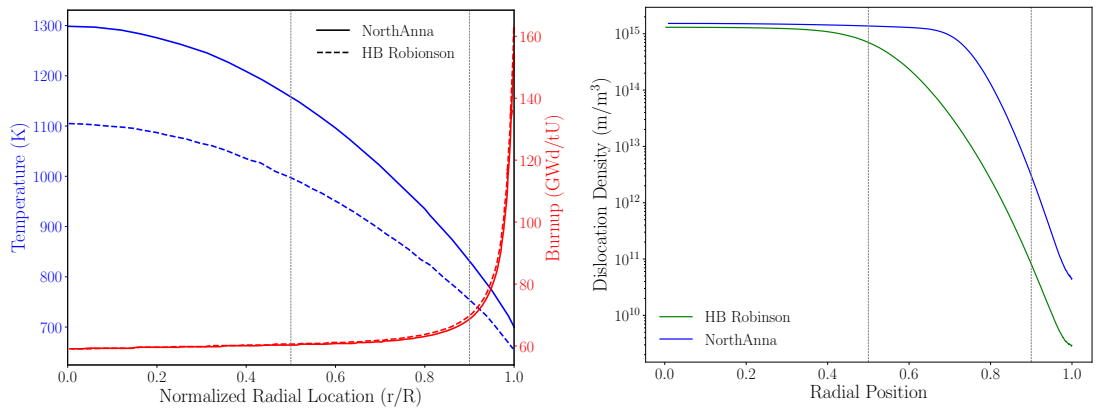

(a) (b)

Figure 19. (a) Radial temperature and burnup variation obtained from two different experiments. (b) Radial variation in dislocation density following Rest model corresponding to two different temperature profiles.

to be $\varepsilon_i = 1.975$ eV [34]. The prefactor D_i^0 was calculated using Reference [34]

$$D^0 = \frac{w j_d^2 j_s}{6}, \tag{31}$$

where w is the attempt (vibrational) frequency, j_d is the jump distance, and j_s is the number of jump sites. Using $w = 5.45$ THz, $j_d = a/2$, and $j_s = 6$ [34], $D_i^0 = 4.08 \times 10^{-7}$ m^2/s. For U-site vacancies V_u, $\varepsilon_v = 4.233$ eV [34]. The prefactor for vacancies was calculated using $w = 1.42$ THz, $j_d = a\sqrt{2}/2$, and $j_s = 12$ [34] to be $D_v^0 = 4.25 \times 10^{-7}$ m^2/s. The recombination distance was estimated as $r_{iv} = j_d Z$ [34], where $j_d = a/2$ is the jump distance for interstitials and $Z \approx 100$, resulting in $r_{iv} = 27.35$ nm. The damage rate K was taken to be $K = 1$ dpa/day [10] or $K = 1.15 \times 10^{-5}$ dpa/s. The updated values used are given in Table 4.

The dislocation density evolution model with this updated set of parameters was run at $T = 953$ K. Comparing the predictions of this model, shown in Figure 20, with the model shown in Figure 16a, it can be seen that the updated set of parameters causes the model to under-predict dislocation density evolution by several orders of magnitude.

3.2.4. Fit to Match Experimental Dislocation Density Data

Given that the initial set of model parameters did not match the experimental data well, and substituting more recently determined parameters as shown in Table 4 did not improve agreement, a fit to the data of Reference [6] was performed using the `curve_fit` function from the SciPy Optimize module. To provide a more realistic starting condition for the fit, an initial dislocation density $\rho_0 = 10^{12}$ m/m^3 was assumed at zero burnup, and was added to Equation 25. Some parameters that are well known, such as a, b_v, and ν, were left at the same values as shown in Table 4. D_i^0 and D_v^0 were also left at the values used in Table 4 because they did not affect the fit results as significantly as other values and were of a typically expected order of magnitude for diffusion prefactors. The parameters obtained in the fitting process are shown in Table 5. Although the values obtained for ε_i and Z_{iv} are physically reasonable, the vacancy activation energy of $\varepsilon_v = 0.8$ eV obtained from the fit is very low compared to the value calculated by density functional theory of 4.233 eV [34]. Additionally, the vacancy-interstitial recombination distance obtained from the fit

Parameter	Value	Reference
D_i^0	4.08×10^{-7} m^2/s	[34]
D_v^0	4.25×10^{-7} m^2/s	[34]
ε_i	1.975 eV	[34]
ε_v	4.233 eV	[34]
r_{iv}	27.35 nm	[34]
Z_{iv}	5×10^{-4}	[30]
a	0.547 nm	[32]
b_v	$\sqrt{2}a/2$	[32]
K	1.15×10^{-5} dpa/s	[10]
ν	0.345	[33]
Ω	$a^3/4$	[7]

Table 4. Updated parameters used for dislocation density evolution model in Figure 20, taken from more recent values from the literature.

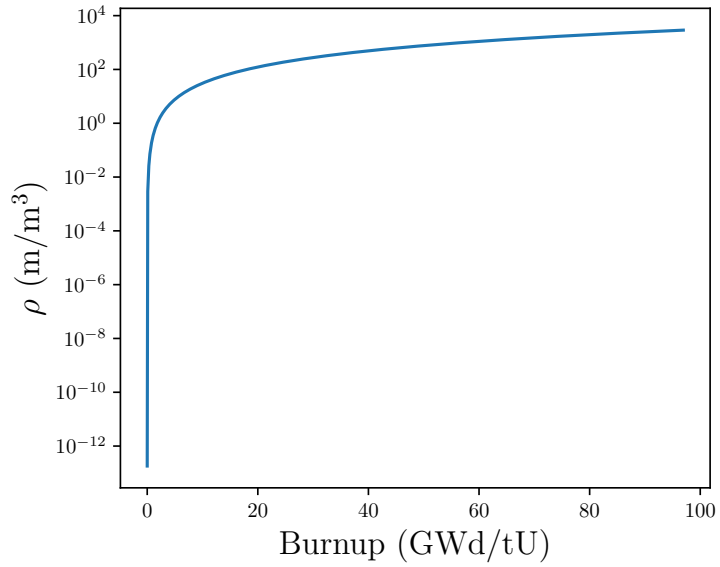

Figure 20. Dislocation density evolution at 953 K using the model of Reference [7], updated with parameters shown in Table 4 (taken from more recent literature values).

Parameter	Value	Reference
D_i^0	4.08×10^{-7} m^2/s	[34]
D_v^0	4.25×10^{-7} m^2/s	[34]
ε_i	0.6 eV	fit
ε_v	0.8 eV	fit
r_{iv}	9.3 mm	fit
Z_{iv}	5.6×10^{-3}	fit
a	0.547 nm	[32]
b_v	$\sqrt{2}a/2$	[32]
K	1.15×10^{-5} dpa/s	[10]
ν	0.345	[33]
Ω	$a^3/4$	[7]

Table 5. Parameters obtained by fitting dislocation density evolution model to data of Reference [6].

of $r_{iv} = 9.5$ mm is many orders of magnitude greater than expected; r_{iv} would typically be expected to be in the range of nm to tens of nm.

The results of the fit at 953 K are shown together with the experimental data on which the fit was based (also at 953 K) in Figure 21, along with results at lower temperatures of 800 K and 700 K. Consistent with the results obtained in the parametric study earlier in this section, ρ_N increases more slowly at lower temperatures.

The effect of increasing fission rate by a factor of 3 from its initial value $\dot{F}_0$ for 700 K is also shown in Figure 21 as $\dot{F}/\dot{F}_0 = 3$. This is representative of conditions typically found in the rim of UO_2 fuel in LWRs. In this case, ρ_N increases more slowly with respect to burnup than the case with $\dot{F}_0$. This is because $K \propto \dot{F}$ in Equation 28, meaning that there are more interstitials created from which loops can be formed as $\dot{F}$ increases. However, since $c_i \propto \sqrt{K}$ in Equation 28, but burnup is linearly proportional to $\dot{F}$, c_i increases more slowly with increasing $\dot{F}$ than burnup, so ρ_N increases more slowly with increased burnup for the case $\dot{F}/\dot{F}_0 = 3$. This behavior is contrary to what would be expected based on experimental observations of the rim (assuming rim region restructuring is driven by dislocation accumulation and subsequent polygonization). Since the rim experiences restructuring earlier and to a great extent than the "dark zone" of high burnup pellets, it should be expected that dislocation density for the 700 K, $\dot{F}/\dot{F}_0 = 3$ case should increase above the higher-temperature cases somewhere prior to 100 GWd/tU.

3.2.5. Evaluation of Defect Sink Impact on Model Performance

Given the failure of the model of Reference [7] to reproduce experimental observations, the assumptions that led to derivation of the model need to be assessed. One assumption in the model is that interstitial and vacancy sinks can be neglected in determining the interstitial concentration by Equation 28. Here, we consider the effect of including sinks on the predicted interstitial concentration to determine whether the neglect of sinks is a valid assumption, with particular focus on lower temperatures such as experienced in the rim region of commercial LWR fuel pellets. When interstitial and vacancy sinks are included, Equation 28 needs to be replaced by the expression [35]

$$c_i^{ss} = \frac{-k_s D_i D_v + \sqrt{(k_s D_i D_v)^2 + 4 k_{iv} K D_i D_v}}{2 k_{iv} D_i}, \tag{32}$$

where k_s is the sink strength (assumed to be the same for interstitials and vacancies) and $k_{iv} = \frac{4\pi r_{iv}(D_i + D_v)}{\Omega}$.

The interstitial concentrations obtained by Equations 28 (no sinks) and 32 (with sinks) are compared in Figure 22a, using the baseline parameters of the model given in Table 3. A value of $k_s = 1.75 \times 10^{13}$

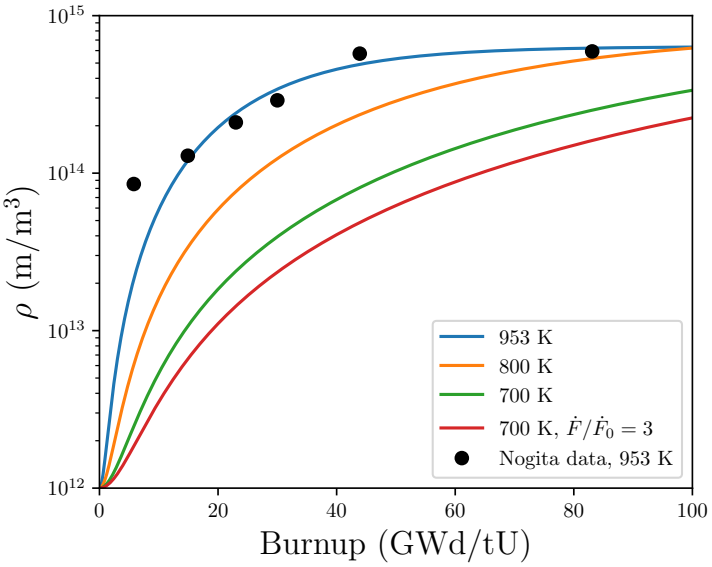

Figure 21. Dislocation density evolution at 953 K using the model of Reference [7], updated with parameters shown in Table 5 based on fit to data of Reference [6].

m/m^3 was chosen for the sink strength assuming that dislocations are the dominant sinks for vacancies and interstitials, and that sink strength is of the same order of magnitude as the dislocation density [35]. The choice of $k_s = 1.75 \times 10^{13}$ m/m^3 thus represents early stage conditions based on dislocation densities in Figure 16a. Very little deviation is observed between the no-sinks and with-sinks cases, particularly at low temperatures. The inclusion of sinks is therefore not likely to be an important factor at very low burnups.

The case of higher burnups is considered in Figure 22b, where $k_s = 1.75 \times 10^{14}$ m/m^3 is assumed due to the higher dislocation density at higher burnup. In this case, a more significant deviation between the no-sinks and with-sinks behavior is seen at higher temperatures. However, the behavior at $T = 700$ K is unchanged, meaning that the behavior of dislocation accumulation in the rim, where the model behavior is most problematic, is not affected by the inclusion of dislocation sinks.

As shown in Table 4, more recent estimates put the damage rate K lower, with $K = 1.15 \times 10^{-5}$ dpa/s rather than $K = 2 \times 10^{-4}$ dpa/s as used in Reference [7], Figure 22a, and Figure 22b. The steady-state interstitial concentrations without and with sinks are shown using $K = 1.15 \times 10^{-5}$ dpa/s in Figure 22c. Here, the interstitial concentration is lower everywhere, and there is greater deviation between the no-sinks and with-sinks cases than in Figure 22b at higher temperatures. However, the interstitial concentration at 700 K is unaffected by the presence of sinks. Thus, the inclusion of dislocation sinks is not seen to be a potential explanation for the failure of the model at conditions representative of the rim of LWR UO_2 fuel.

3.2.6. Summary and Future Work

The dislocation density evolution model of Reference [7] was thoroughly investigated. Two independent implementations of the model in its published form gave predicted dislocation densities that did not agree with the published model results but were consistent with each other. The most likely explanation is an error in the implementation of the model or the model parameters provided in the original published paper. Use of updated parameters for the model based on more recent values from the literature did not improve agreement with experimental data. A fit of the model parameters that enabled the model to match experimental data [6] resulted in unphysical values of some model parameters. The model in its current form also cannot explain

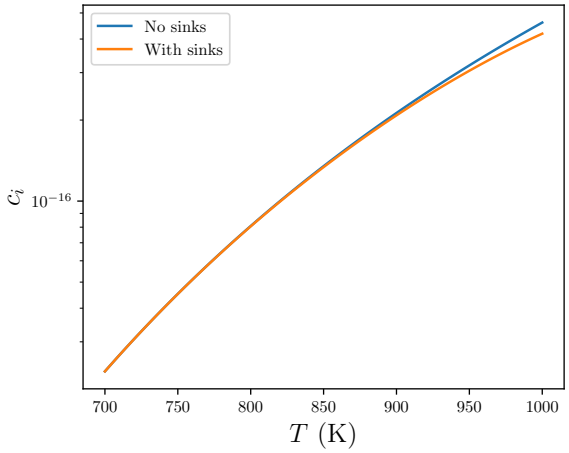

(a) $K = 2 \times 10^{-4}$ dpa/s, $k_s = 1.75 \times 10^{13}$ m/m^3

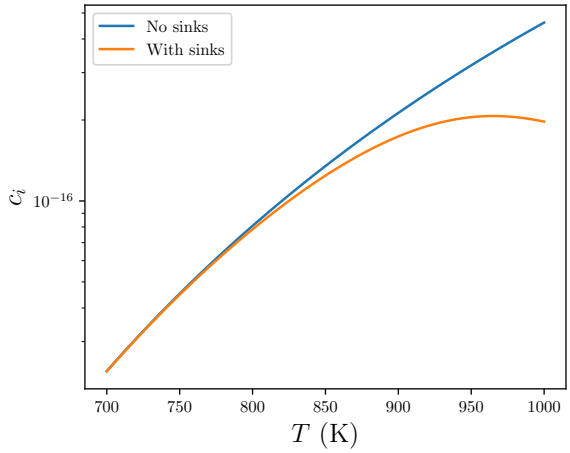

(b) $K = 2 \times 10^{-4}$ dpa/s, $k_s = 1.75 \times 10^{14}$ m/m^3

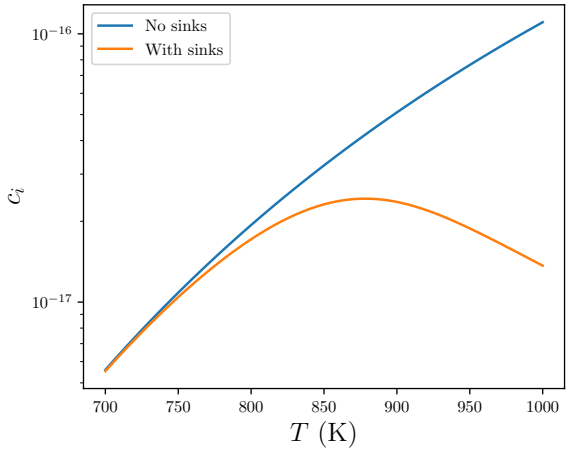

(c) $K = 1.15 \times 10^{-5}$ dpa/s, $k_s = 1.75 \times 10^{14}$ m/m^3

Figure 22. Interstitial concentrations as a function of temperature as predicted for the case with no sinks (Equation 28) and for the case with sinks (Equation 32). The inclusion of sinks does not affect the model behavior at the lower temperatures (700 K) where the model performance is most problematic.

the increased dislocation density and resulting early restructuring in the rim region.

To understand why the model does not match experimental data, efforts were made to understand the impact of the model's assumptions. The impact of the model's neglect of defect sinks was evaluated by calculating interstitial concentration with defect sinks and comparing it to the values obtained without them. The presence of defect sinks may affect the model's behavior at higher temperatures but does not account for the failure to predict rim-region behavior. The testing performed assumed that the sink strength coefficient k_s was the same for vacancies and interstitials; this assumption should be relaxed in future work. The impact of the form of the dislocation creation and annihilation terms (first and second terms on the right-hand side of Equation 22, respectively) should also be assessed in future work. The creation term is proportional to $\rho_N^{1/2}$ through Equation 24. However, proportionality to ρ_N [36] has also been proposed, as well as more detailed approaches to creation [37, 38]. The annihilation term in Equation 22 is proportional to $\rho^{3/2}$. However, dependence on ρ^2 [37] and ρ [38] has also been proposed in the literature. In future work, dependencies should be determined that allow a dislocation evolution model that better matches experimental data for UO_2.

4. FRAGMENTATION IN THE DARK ZONE

4.1. Phase-field Fracture Model

The phase-field fracture model is formulated based on the mechanics minimization problem that is regularized and approximated using the phase-field variable c, given by

$$\{\boldsymbol{u}, c\} = \arg\min_{\boldsymbol{u},c} \Psi(\boldsymbol{u}, \boldsymbol{\nabla u}, c, \boldsymbol{\nabla} c), \tag{33a}$$

$$\text{subject to} \qquad \boldsymbol{u} = \boldsymbol{g}, \quad \forall \boldsymbol{x} \in \partial\Omega_D, \tag{33b}$$

$$\dot{c} \geqslant 0, \quad \forall \boldsymbol{x} \in \Omega, \tag{33c}$$

where u is the displacement vector. Equation (33c) represents the irreversibility condition equivalent to the "no healing" condition on the permanent crack set. The objective function $\Psi(\boldsymbol{u}, \boldsymbol{\nabla u}, c, \boldsymbol{\nabla} c)$ is defined as

$$\begin{aligned}\Psi(\boldsymbol{u}, \boldsymbol{\nabla u}, c, \boldsymbol{\nabla} c) =& \Psi_{\text{elastic}}(\boldsymbol{\nabla u}, g(c)) + \Psi^{l}_{\text{fracture}}(c, \boldsymbol{\nabla} c) - \Psi_{\text{dissipation}}(c) \\ &- \Psi^{\text{traction}}_{\text{external}}(\boldsymbol{u}) - \widetilde{\Psi}^{\text{pressure}}_{\text{external}}(\boldsymbol{u}, c, \boldsymbol{\nabla} c),\end{aligned} \tag{34a}$$

$$\Psi_{\text{elastic}}(\boldsymbol{\nabla u}, g(c)) = \int_{\Omega} g(c)\psi^{\langle \text{A} \rangle}_{\text{elastic}}(\boldsymbol{\nabla u})\, \mathrm{d}V + \int_{\Omega} \psi^{\langle \text{I} \rangle}_{\text{elastic}}(\boldsymbol{\nabla u})\, \mathrm{d}V, \tag{34b}$$

$$\Psi^{l}_{\text{fracture}}(c, \boldsymbol{\nabla} c) = \int_{\Omega} \mathcal{G}_c \gamma_l(c, \boldsymbol{\nabla} c)\, \mathrm{d}V, \tag{34c}$$

$$\dot{\Psi}_{\text{dissipation}}(\dot{c}) = \int_{\Omega} \frac{1}{2}\eta \dot{c}^2\, \mathrm{d}V, \tag{34d}$$

$$\Psi^{\text{traction}}_{\text{external}}(\boldsymbol{u}) = \int_{\partial\Omega_N} \boldsymbol{\tau} \cdot \boldsymbol{u}\, \mathrm{d}A, \tag{34e}$$

$$\widetilde{\Psi}^{\text{pressure}}_{\text{external}}(\boldsymbol{u}, c, \boldsymbol{\nabla} c) = -\int_{\Omega} p \boldsymbol{\nabla} c \cdot \boldsymbol{u} I'(c)\, \mathrm{d}V. \tag{34f}$$

It considers the energy contribution due to deformation (Ψ_{elastic}), fracture ($\Psi^{l}_{\text{fracture}}$, internal dissipation ($\Psi_{\text{dissipation}}$), and external pressure ($\Psi^{\text{traction}}_{\text{external}}$, $\widetilde{\Psi}^{\text{pressure}}_{\text{external}}$). Let us define the trial spaces, as follows

$$\mathcal{U} = \left\{ \boldsymbol{u} | \boldsymbol{u} \in \mathcal{H}^1(\Omega)^d, \boldsymbol{u} = \boldsymbol{g}, \forall \boldsymbol{x} \in \partial\Omega \right\}, \quad \mathcal{C} = \left\{ c | c \in \mathcal{H}^1(\Omega), \dot{c} \geqslant 0, \forall \boldsymbol{x} \in \Omega \right\}, \tag{35}$$

along with their corresponding weighting spaces,

$$\mathcal{V} = \left\{ \delta\boldsymbol{u} | \delta\boldsymbol{u} \in \mathcal{H}^1(\Omega)^d, \boldsymbol{u} = \boldsymbol{0}, \forall \boldsymbol{x} \in \partial\Omega \right\}, \quad \mathcal{Q} = \left\{ \delta c | \delta c \in \mathcal{H}^1(\Omega), \delta c \geqslant 0, \forall \boldsymbol{x} \in \Omega \right\}. \tag{36}$$

The optimality conditions for $\boldsymbol{u}$ follow from the functional derivative of the objective function Ψ, given by

$$\begin{aligned}&\int_{\Omega} \boldsymbol{\nabla} \cdot \frac{\partial \psi_{\text{elastic}}(\boldsymbol{\nabla u}, g(c))}{\partial \boldsymbol{\nabla u}}\, \mathrm{d}V - \int_{\partial\Omega_N} \frac{\partial \psi_{\text{elastic}}(\boldsymbol{\nabla u}, g(c))}{\partial \boldsymbol{\nabla u}} \boldsymbol{n}\, \mathrm{d}A \\ &+ \int_{\partial\Omega_N} \frac{\partial \psi^{\text{traction}}_{\text{external}}(\boldsymbol{u})}{\partial \boldsymbol{u}}\, \mathrm{d}A + \int_{\Omega} \frac{\partial \widetilde{\psi}^{\text{pressure}}_{\text{external}}(\boldsymbol{u}, c, \boldsymbol{\nabla} c)}{\partial \boldsymbol{u}}\, \mathrm{d}V = 0, \quad \forall \Omega' \subseteq \Omega, \forall \partial\Omega'_N \subseteq \partial\Omega_N.\end{aligned} \tag{37}$$

Substituting (34) yields

$$\boldsymbol{\nabla}\cdot\boldsymbol{\sigma} - pI'(c)\boldsymbol{\nabla}c = \boldsymbol{0}, \quad \forall \boldsymbol{x}\in\Omega, \tag{38a}$$

$$\boldsymbol{\sigma}\boldsymbol{n} = \boldsymbol{\tau}, \quad \forall \boldsymbol{x}\in\Omega_N, \tag{38b}$$

where $\boldsymbol{\sigma} = \dfrac{\partial \psi_{\text{elastic}}}{\partial \boldsymbol{\nabla} \boldsymbol{u}}$ is the stress-strain constitutive relation. The optimality conditions for c that are subject to the irreversibility constraint (33c) also follow from the functional derivative (with respect to the rate of the objective function) and recover the Karush–Kuhn–Tucker conditions, such that

$$\begin{aligned}
&\int_\Omega \frac{\partial \psi_{\text{elastic}}(\boldsymbol{\nabla}\boldsymbol{u}, g(c))}{\partial c}\dot{c}\,\mathrm{d}V - \int_\Omega \boldsymbol{\nabla}\cdot\frac{\partial \psi^l_{\text{fracture}}(c,\boldsymbol{\nabla}c)}{\partial \boldsymbol{\nabla}c}\dot{c}\,\mathrm{d}V + \int_{\partial\Omega}\frac{\partial \psi^l_{\text{fracture}}(c,\boldsymbol{\nabla}c)}{\partial \boldsymbol{\nabla}c}\cdot\boldsymbol{n}\dot{c}\,\mathrm{d}A \\
&+\int_\Omega \frac{\partial \psi^l_{\text{fracture}}(c,\boldsymbol{\nabla}c)}{\partial c}\dot{c}\,\mathrm{d}V + \int_\Omega \boldsymbol{\nabla}\cdot\frac{\partial \widetilde{\psi}^{\text{pressure}}_{\text{external}}(c,\boldsymbol{\nabla}c)}{\partial \boldsymbol{\nabla}c}\dot{c}\,\mathrm{d}V - \int_{\partial\Omega}\frac{\partial \widetilde{\psi}^{\text{pressure}}_{\text{external}}(c,\boldsymbol{\nabla}c)}{\partial \boldsymbol{\nabla}c}\cdot\boldsymbol{n}\dot{c}\,\mathrm{d}A \\
&+\int_\Omega \frac{\partial \widetilde{\psi}^{\text{pressure}}_{\text{external}}(c,\boldsymbol{\nabla}c)}{\partial c}\dot{c}\,\mathrm{d}V + \int_\Omega \frac{\partial \dot{\psi}_{\text{dissipation}}(\dot{c})}{\partial \dot{c}}\dot{c}\,\mathrm{d}V = 0, \quad \forall\Omega'\subseteq\Omega, \forall\partial\Omega'_N\subseteq\partial\Omega_N.
\end{aligned} \tag{39}$$

Again, substituting (34) yields

$$\begin{aligned}
&\phi^f \geqslant 0, \quad \dot{c}\geqslant 0, \quad \phi^f\dot{c} = 0, \\
&\text{with } \phi^f = \begin{cases} \eta\dot{c} - \boldsymbol{\nabla}\cdot\boldsymbol{\xi} + \dfrac{\mathcal{G}_c}{c_0 l}\alpha'(c) - Y, & \forall \boldsymbol{x}\in\Omega, \\ \boldsymbol{\xi}\cdot\boldsymbol{n} + pI'(c)\boldsymbol{u}\cdot\boldsymbol{n}, & \forall\boldsymbol{x}\in\partial\Omega \end{cases},
\end{aligned} \tag{40}$$

where $\boldsymbol{\xi} = \dfrac{\partial \psi^l_{\text{fracture}}}{\partial \boldsymbol{\nabla}c} = \dfrac{2\mathcal{G}_c l}{c_0}\boldsymbol{\nabla}c$ is the thermodynamic conjugate to $\boldsymbol{\nabla}c$, and Y is the generalized fracture driving force consisting of contributions from the active elastic energy density as well as work done by pressure

$$Y = -g'(c)\psi^{\langle \mathrm{A}\rangle}_{\text{elastic}} + pI'(c)\boldsymbol{\nabla}\cdot\boldsymbol{u}. \tag{41}$$

With a view toward the solution strategy, using a variational inequality solver (e.g., a primal-dual active set algorithm) to enforce the irreversibility constraint requires discretization of the fracture envelope ϕ^f only on the inactive sets $\dot{c} > 0$ and $\phi^f = 0$. Hence, only the weak form in the case of $\phi^f = 0$ is outlined below.

Given $\boldsymbol{g}$, $\boldsymbol{\tau}$, and c_0, find $\boldsymbol{u}\in\mathcal{U}$ and $c\in\mathcal{C}$, such that $\forall\delta\boldsymbol{u}\in\mathcal{V}$ and $\forall\delta c\in\mathcal{Q}$,

$$\int_\Omega \boldsymbol{\sigma} : \boldsymbol{\nabla}\delta\boldsymbol{u}\,\mathrm{d}V + \int_\Omega pI'(c)\boldsymbol{\nabla}c\cdot\delta\boldsymbol{u}\,\mathrm{d}V - \int_{\partial\Omega_N}\boldsymbol{\tau}\cdot\delta\boldsymbol{u}\,\mathrm{d}A = 0, \tag{42a}$$

$$\int_\Omega \eta\dot{c}\delta c\,\mathrm{d}V + \int_\Omega \boldsymbol{\xi}\cdot\boldsymbol{\nabla}\delta c\,\mathrm{d}V + \int_\Omega \frac{\mathcal{G}_c}{c_0 l}\alpha'(c)\delta c\,\mathrm{d}V - \int_\Omega Y\delta c\,\mathrm{d}V + \int_{\partial\Omega} pI'(c)\boldsymbol{u}\cdot\boldsymbol{n}\delta c\,\mathrm{d}A = 0. \tag{42b}$$

Furthermore, the macro-scale pulverization behavior is approximated by using periodic boundary conditions (PBC). PBCs are useful for avoiding the boundary effects caused by finite size and for making the system deform like an infinite one. In Multiphysics Object-Oriented Simulation Environment (MOOSE), the global strain system was implemented to enforce thePBC [39]. The global strain system can capture the deformation with applied loads while still maintaining the periodic strains.

4.2. Mesoscale Fragmentation Results

In FY 2025, the phase-field fracture model for quasi-brittle fracture with pressurized bubbles has been extended to the dark zone. To simulate the fragmentation behavior in the dark zone, we start by initializing the microstructure from the mesoscale simulations presented in Section 2. The model is updated to use the MD-informed fracture stress and energy release rate for grain boundaries [40]. Furthermore, the temperature effect is included in the simulations. A typical LOCA test usually ramps the temperature at a rate of 5 K/sec. In this case to reduce the computational cost, we use a linear temperature ramp rate of 10 K/sec. This speeds up the simulations without affecting the critical stress at which the fracture occurs. The critical fracture stress of the material decreases with increasing temperatures [41, 42].

Figure 23a shows the crack propagation captured using the phase-field fracture simulations performed on two dark-zone-specific initial conditions. Two grain morphologies with different restructuring stages and grain sizes have been selected in this case. In both cases, crack propagation initiates from the larger bubble and similar crack growth patterns are observed. Formation of new GBs due to grain subdivision weakens the material and creates a GB network that facilitates crack propagation leading to fragmentation. The critical bubble pressure and temperature at which pulverization occurs are similar for both the cases presented here. This indicates that the fragmentation is primarily governed by the operating conditions and bubble pressure, rather than restructuring fraction and grain sizes. Here, the fragmentation criteria is defined by the crack initiation, rather than a crack propagation criteria. Table 6 lists the critical stress and temperature at which fragmentation begins under LOCA conditions for different external pressure. It is observed that critical bubble pressure at which fragmentation occurs increases with increasing external pressure. The critical pressure inputs will be provided to BISON for further fuel performance assessments.

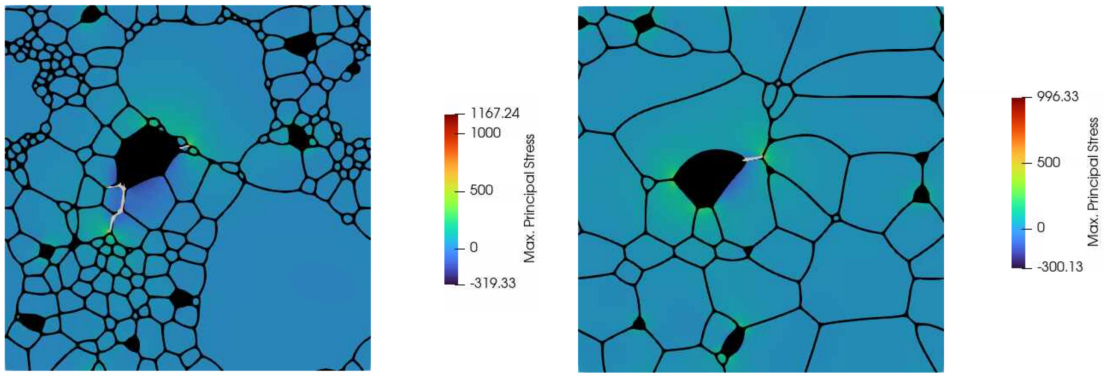

(a) (b)

Figure 23. Fracture behavior in the dark zone with no eternal pressure.

Simulation	External Pressure (MPa)	Temperature (K)	Critical Fracture Stress (MPa)	Critical Bubble Pressure (MPa)
Case I	0 30 60	1260 1300 1340	296.77 255.66 217.46	160.0 171.43 182.86
Case II	0 30 60	1250 1290 1330	307.5 265.67 226.74	157.14 168.57 180.0

Table 6. Fragmentation criteria from the phase-field fracture simulations using dark zone microstructures.

5. CONCLUSION

In conclusion, we present a novel phase-field model for predicting the restructuring observed in high burnup UO_2 fuel. We demonstrated how different parameters such as burnup rate and temperature influence the subgrain formation rate and restructuring predicted at the mesoscale. The key characteristics demonstrated by the model are as follows:

- Subgrain formation begins around existing fission gas bubbles, then proceeds toward triple junctions, grain boundaries, and grain interiors.
- A restructuring bias is observed within the microstructure, due to variation in dislocation density among different grains.
- The rate of restructuring increases with an increase in initial dislocation density, rate of dislocation accumulation, and subgrain formation rate.
- The rate of restructuring and the average grain diameter decrease with decreasing fuel temperature.
- The restructuring occurs faster with higher burnup rates, resulting in smaller grain sizes.

The model presented in this work can be used to simulate the restructuring observed in different radial locations of the fuel (dark zone vs. rim regions) by choosing appropriate initial microstructural characteristics, temperatures, and burnup rates (Figure 24).

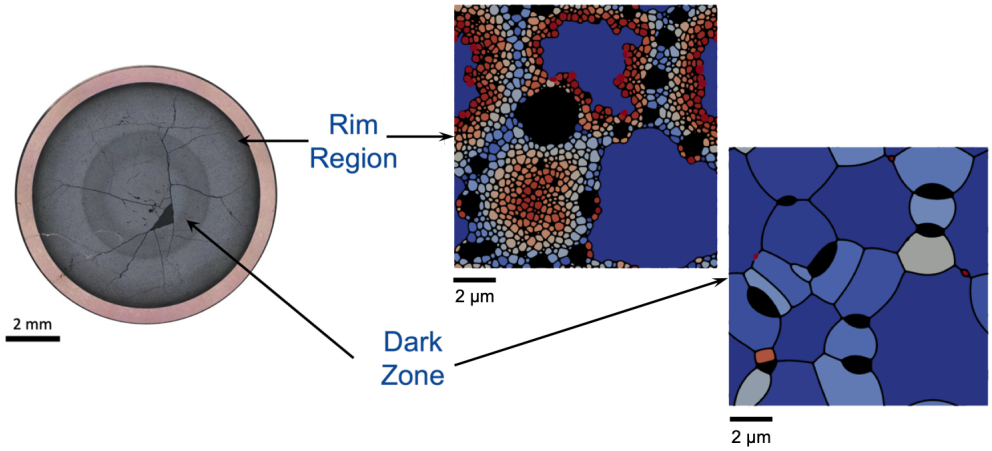

Figure 24. Restructuring along fuel radius demonstrated with simulated microstructures representing morphologies observed in different radial zones.

Based on the mesoscale simulations, a mechanistic model for restructuring and grain size evolution was implemented in BISON. Thus, this work provides a first-of-its-kind restructuring model for different regions of high burnup fuel to BISON. It was shown that the model predicts similar microstructural characteristics and grain size evolution along fuel radius as those observed in experiments. This model enables BISON to appropriately assess the effect of restructuring on the transient fission gas release (tFGR). However, there are some limitations of the current work that should be addressed in future work. The model currently assumes that the restructuring begins with the formation of subgrains, and does not distinguish between subgrains with LAGBs and those with HAGBs (as observed in different regions of the fuel). Additionally, the subgrain formation criteria rely on a predefined subgrain size and geometric factors derived from experimental observations. It is noteworthy that despite these limitations, the model realistically captures the grain morphologies and average grain sizes, as evidenced by comparison with experimental results. The generated microstructures can be used to assess the properties and performance of the restructured fuel [28, 43].

The mesoscale restructuring model currently uses an isotropic empirical correlation for burnup-dependent dislocation evolution, which fails to account for the effects of grain orientation, fission rate, and temperature. To address these limitations, a more mechanistic multiscale approach is necessary. A mechanistic model for dislocation density from the literature [7] was evaluated; however, the model failed to match experimental data. Based on this, future work will consider different physical forms for dislocation creation and annihilation, as has been proposed in other work for materials other than UO_2.

Finally, phase-field fracture simulations with dark-zone-specific microstructures were presented to provide the fragmentation criteria for the dark zone. This provides a critical link from microstructure to performance that is especially relevant for stakeholders concerned about fuel fragmentation, relocation, and dispersal. However, future work is needed to implement this dark zone fracture criteria in BISON and validate it using integral fuel irradiation. The current modeling approach also assumes that the fracture properties calculated using atomistic methods for rim-region high-angle grain boundaries are also applicable for the lower grain boundary angles typically found in the dark zone. This assumption should be tested through additional future atomistic calculations.

6. REFERENCES

[1] C. McKinney, C. Parish, J. Werden, T. Gerczak, J. Harp, L. Reyes, N. Capps, Advanced multiscale microscopy characterization of high burnup lwr uo2 before and after loca testing, Tech. rep. (2023).

[2] N. Capps, D. Schappel, C. McKinney, J. Harp, M. Cooper, D. Andersson, P. Simon, S. Novascone, Bison validation against pressurized water reactor high-burnup post-irradiation examination data, in: Proceedings of Top Fuel 2024, Grenoble, France, 2024.

[3] Plotdigitizer: Version 3.1.5 (2024).
URL https://plotdigitizer.com

[4] T. J. Gerczak, C. M. Parish, P. D. Edmondson, C. Balswin, K. A. Terrani, Restructuring in high burnup uo2 studied using modern electron microscopy, J. Nucl. Mat. 509 (2018) 246–259. doi:https://doi.org/10.1016/j.jnucmat.2018.05.077.

[5] C. McKinney, R. Seibert, J. Werden, C. Parish, J. Werden, T. Gerczak, J. Harp, N. Capps, Characterization of the radial microstructural evolution in lwr uo2 using electron backscatter diffraction, Journal of Nuclear Materials 585 (2023) 154605. doi:https://doi.org/10.1016/j.jnucmat.2023.154605.

[6] K. Nogita, K. Une, Radiation-induced microstructural change in high burnup UO_2 fuel pellets, Nuclear Instruments and Methods in Physics Research Section B: Beam Interactions with Materials and Atoms 91 (1-4) (1994) 301–306.

[7] J. Rest, Derivation of analytical expressions for the network dislocation density, change in lattice parameter, and for the recrystallized grain size in nuclear fuels, Journal of Nuclear Materials 349 (1) (2006) 150–159. doi:https://doi.org/10.1016/j.jnucmat.2005.10.007.
URL https://www.sciencedirect.com/science/article/pii/S0022311505005015

[8] K. J. Geelhood, Fuel performance considerations and data needs for burnup above 62 gwd/mtu (2019).

[9] F. Pimentel, F. Smith, The economic benefits and challenges with utilizing increased enrichment and fuel burnup for light□water reactors, Tech. rep., Nuclear Energy Institute (2019).

[10] V. V. Rondinella, T. Wiss, The high burn-up structure in nuclear fuel, Materials Today 13 (2010) 24–32.

[11] J. Noirot, I. Zacharie-Aubrun, T. Blay, Focused ion beam scanning electron microscope examination of high burn-up uo2 in the center of a pellet, Nuclear Engineering and Technology 50 (2018) 259–267. doi:https://doi.org/10.1016/j.net.2017.12.002.

[12] U. N. R. C. (NRC), Ril 2021-13, interpretation of research on fuel fragmentation, relocation, and dispersal at high burnup (2021).

[13] H. Matzke, On the rim effect in high burnup uo2 lwr fuels, J. Nucl. Mat. 189 (1992) 141–148.

[14] N. Capps, C. Jensen, F. Cappia, J. Harp, K. Terrani, N. Woolstenhulme, D. Wachs, A critical review of high burnup fuel fragmentation, relocation, and dispersal under loss-of-coolant accident conditions, Journal of Nuclear Materials 546 (2021) 152750. doi:https://doi.org/10.1016/j.jnucmat.2020.152750.

[15] Z. Xiao, Y. Wang, S. Hu, Y. Li, S.-Q. Shi, A quantitative phase-field model of gas bubble evolution in UO_2, Computational Materials Science 184 (2020) 109867.

[16] C. Smith, S. Biswas, B. D. Miller, B. Kombaiah, D. Frazer, D. D. Keiser, A. Aitkaliyeva, Investigation of high burnup structure in u-mo fuels, Journal of Nuclear Materials 563.

[17] T. Wiss, V. V. Rondinella, R. J. M. Konings, D. Staicu, D. Papaioannou, S. Bremier, P. Pöml, O. Benes, J.-Y. Colle, P. V. Uffelen, A. Schubert, F. Cappia, M. Marchetti, D. Pizzocri, F. Jatuff, W. Goll, T. Sonoda, A. Sasahara, S. Kitajima, M. Kinoshita, Properties of the high burnup structure in nuclear light water reactor fuel.

[18] F. Cappia, K. Wright, D. Frazer, K. Bawane, B. Kombaiah, W. Williams, S. Finkeldei, F. Teng, J. Giglio, M. Cinbiz, B. Hilton, J. Strumpell, R. Daum, K. Yueh, C. Jensen, D. Wachs, Detailed characterization of a pwr fuel rod at high burnup in support of loca testing, Journal of Nuclear Materials 569 (2022) 153881. doi:https://doi.org/10.1016/j.jnucmat.2022.153881.
URL https://www.sciencedirect.com/science/article/pii/S0022311522003671

[19] M. Kinoshita, Towards the mathematical model of rim structure formation, J. Nucl. Mat. 248 (1997) 185–190.

[20] J. Rest, A model for the influence of microstructure, precipitate pinning and fission gas behavior on irradiation-induced recrystallization of nuclear fuels, Journal of Nuclear Materials 326 (2) (2004) 175–184. doi:https://doi.org/10.1016/j.jnucmat.2004.01.009.
URL https://www.sciencedirect.com/science/article/pii/S0022311504000327

[21] D. Pizzocri, F. Cappia, L. Luzzi, G. Pastore, V. Rondinella, P. Van Uffelen, A semi-empirical model for the formation and depletion of the high burnup structure in uo2, Journal of Nuclear Materials 487 (2017) 23–29. doi:https://doi.org/10.1016/j.jnucmat.2017.01.053.
URL https://www.sciencedirect.com/science/article/pii/S0022311516307279

[22] T. Barani, D. Pizzocri, F. Cappia, G. Pastore, P. V. Uffelen, Modeling high burnup structure in oxide fuels for application to fuel performance codes. part i: High burnup structure formation, Journal of Nuclear Materials 539 (2020) 152296. doi:https://doi.org/10.1016/j.jnucmat.2020.152296.

[23] S. Biswas, L. K. Aagesen, P.-C. Simon, Phase-field modeling for restructuring in the dark zone of high burnup uo2, Tech. Rep. INL/RPT-24-81091, Idaho National Laboratory (2024).

[24] S. Biswas, L. K. Aagesen, Mesoscale modeling of restructuring in high burnup uo_2 fuel, Comp. Mat. Sci. 258 (114052). doi:https://doi.org/10.1016/j.commatsci.2025.114052.

[25] T. Takaki, Y. Tomita, Static recrystallization simulations starting from predicted deformation microstructure by coupling multi-phase-field method and finite element method based on crystal plasticity, International Journal of Mechanical Sciences 52 (2) (2010) 320–328.

[26] S. Gentry, K. Thornton, Simulating recrystallization in titanium using the phase field method, in: IOP Conference Series: Materials Science and Engineering, Vol. 89, IOP Publishing, 2015, p. 012024.

[27] K. Nogita, K. Une, Irradiation-induced recrystallization in high burnup UO_2 fuel, Journal of Nuclear Materials 226 (3) (1995) 302–310. doi:10.1016/0022-3115(95)00123-9.

[28] P.-C. A. Simon, K. A. Gamble, A. Pagani, I. T. Ferguson, D. Schwen, L. H. Harbour, L. K. Aagesen Jr, S. R. Novascone, N. Capps, M. W. D. Cooper, C. Matthews, D. Andersson, Deployment of bison models of fuel restructuring at high burnup and related fission gas behavior in uo2doi:10.2172/2472822.
URL https://www.osti.gov/biblio/2472822

[29] J. D. Hales, K. A. Gamble, B. W. Spencer, S. R. Novascone, G. Pastore, W. Liu, D. S. Stafford, R. L. Williamson, D. M. Perez, R. J. Gardner, BISON users manual, Tech. Rep. INL/MIS-13-30307, Rev. 3, Idaho National Laboratory (September 2015).

[30] J. Rest, G. L. Hofman, An alternative explanation for evidence that xenon depletion, pore formation, and grain subdivision begin at different local burnups, Journal of Nuclear Materials 277 (2-3) (2000) 231–238. doi:10.1016/S0022-3115(99)00201-9.
URL <GotoISI>://WOS:000084960800013

[31] H. Matzke, Diffusion-processes in nuclear-fuels, Journal of the Less-Common Metals 121 (1986) 537–564.
URL <GotoISI>://WOS:A1986E178000066

[32] D. R. Olander, Fundamental aspects of nuclear reactor fuel elements, Technical Information Center, Office of Public Affairs Energy Research and Development Administration, 1976.

[33] J. D. Hales, R. L. Williamson, S. R. Novascone, G. Pastore, B. W. Spencer, D. S. Stafford, K. A. Gamble, D. M. Perez, R. J. Gardner, W. Liu, J. Galloway, C. Matthews, C. Unal, N. Carlson, BISON theory manual, Tech. Rep. INL/EXT-13-29930, Rev. 3, Idaho National Laboratory (September 2016).

[34] C. Matthews, R. Perriot, M. W. D. Cooper, C. R. Stanek, D. A. Andersson, Cluster dynamics simulation of uranium self-diffusion during irradiation in UO_2, Journal of Nuclear Materials 527 (2019) 151787.

[35] G. S. Was, Fundamentals of Radiation Materials Science, Springer, 2010.

[36] W. G. Wolfer, B. B. Glasgow, Dislocation evolution in metals during irradiation, Acta Metallurgica 33 (11) (1985) 1997–2004. doi:10.1016/0001-6160(85)90122-1.
URL <GotoISI>://WOS:A1985ASV4800006

[37] T. Jourdan, Influence of dislocation and dislocation loop biases on microstructures simulated by rate equation cluster dynamics, Journal of Nuclear Materials 467 (2015) 286–301. doi:10.1016/j.jnucmat.2015.09.046.
URL <GotoISI>://WOS:000365602800031

[38] M. Kosmidou, C. Matthews, A. J. Terricabras, H. T. Vo, W. Y. Chen, J. T. White, C. A. Kohnert, D. D. Byler, D. A. Andersson, M. W. D. Cooper, E. Kardoulaki, Temperature dependency of dislocation evolution in kr-irradiated uranium mononitride (un) through tem observation and modeling, Acta Materialia 288. doi:10.1016/j.actamat.2025.120824.
URL <GotoISI>://WOS:001428960400001

[39] S. Biswas, D. Schwen, J. D. Hales, Development of a finite element based strain periodicity implementation method, Finite Elements in Analysis and Design 179. doi:https://doi.org/10.1016/j.finel.2020.103436.

[40] C. O. T. Galvin, D. A. Andersson, M. W. D. Cooper, Characterization of fracture at grain boundary bubbles in uo2 by md simulations, Tech. rep., Los Alamos National Laboratory. (2024).

[41] C. O. T. Galvin, D. A. Andersson, M. W. D. Cooper, Development of fracture criteria for uo2 hbs grain boundaries from atomic scale simulation data for use in meso-scale simulations, Tech. rep., Los Alamos National Laboratory. (2023).

[42] S. Biswas, L. K. Aagesen, W. Jiang, C. O. Galvin, M. W. D. Cooper, Multiscale modeling for high burnup structure formation and associated pulverization, Tech. Rep. INL/RPT-23-74953, Idaho National Laboratory (2023).

[43] W. Jiang, T. Hu, L. K. Aagesen, S. Biswas, K. A. Gamble, A phase-field model of quasi-brittle fracture for pressurized cracks: Application to uo2 high-burnup microstructure fragmentation, Theoretical and Applied Fracture Mechanics 119 (2022) 103348. doi:https://doi.org/10.1016/j.tafmec.2022.103348.
URL https://www.sciencedirect.com/science/article/pii/S0167844222000994